Published in final edited form as:
Neuron. 2018 July 11; 99(1): 147–162.e8. doi:10.1016/j.neuron.2018.05.025.

Persistent Sodium Current Mediates the Steep Voltage Dependence of Spatial Coding in Hippocampal Pyramidal Neurons

Ching-Lung Hsu[1], **Xinyu Zhao**[1], **Aaron D. Milstein**[2], and **Nelson Spruston**[1,*,†]

[1]Janelia Research Campus, Howard Hughes Medical Institute, Ashburn, VA 20147, USA

[2]Neurosurgery Department, Stanford University School of Medicine, Stanford, CA 94305, USA

Summary

The mammalian hippocampus forms a cognitive map using neurons that fire according to an animal's position ('place cells') and many other behavioral and cognitive variables. The responses of these neurons are shaped by their presynaptic inputs and the nature of their postsynaptic integration. In CA1 pyramidal neurons, spatial responses *in vivo* exhibit a strikingly supralinear dependence on baseline membrane potential. The biophysical mechanisms underlying this nonlinear cellular computation are unknown. Here, through a combination of *in-vitro*, *in-vivo*, and *in-silico* approaches, we show that persistent sodium current mediates the strong membrane-potential dependence of place-cell activity. This current operates at membrane potentials below action potential threshold and over seconds-long timescales, mediating powerful—and rapidly reversible—amplification of synaptic responses, which drive place-cell firing. Thus, we identify a biophysical mechanism that shapes the coding properties of neurons composing the hippocampal cognitive map.

eTOC Blurb

The hippocampus encodes experience using 'place cells'. Hsu et al. show that their firing is rapidly and reversibly regulated by small changes in membrane-potential through persistent sodium current, thus providing a biophysical mechanism by which behavior can influence place-cell firing.

---

[*] Correspondence: sprustonn@janelia.hhmi.org.
[†] Lead Contact

Author Contributions
Conceptualization, N.S. and C.-L.H.; Methodology, C.-L.H., X.Z. and A.D.M.; Investigation, C.-L.H., X.Z. and A.D.M.; Formal Analysis, C.-L.H.; Software, C.-L.H., X.Z. and A.D.M.; Data Curation, C.-L.H. and A.D.M.; Visualization, C.-L.H.; Writing, C.-L.H. and N.S.; Project Administration, C.-L.H. and N.S.; Supervision, N.S; Funding Acquisition, N.S.

Declaration of Interests
The authors declare no competing interests.

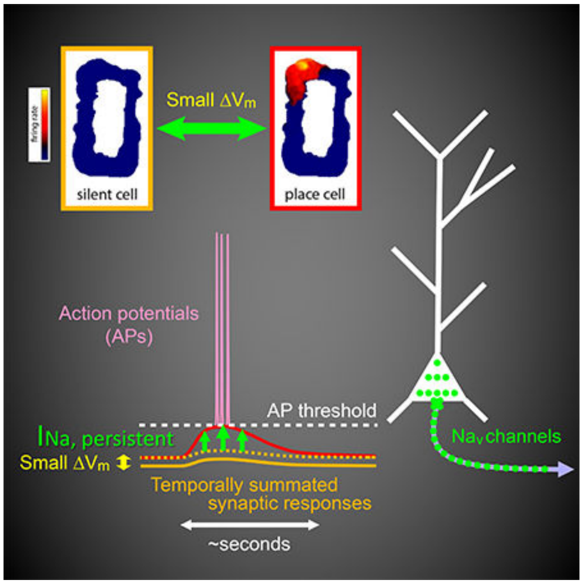

Keywords

Hippocampus; Place cell; Cognitive map; Persistent sodium current; Voltage-gated channels; Synaptic integration

Introduction

Animals respond to survival needs flexibly, in part, through their brain's ability to store and use information about past experiences. A key component of such episodic memories is *where* they occurred. The hippocampus, a mammalian brain structure that is implicated in the formation and storage of episodic memories, is believed to contain such a representation. A set of hippocampal pyramidal neurons—called place cells—collectively encodes the animal's location in a given environment (Derdikman and Knierim, 2014; Eichenbaum et al., 1999; O'Keefe, 1976).

Memories of events consist of information regarding not only place, but also context. Similarly, the firing of hippocampal pyramidal neurons correlates with place as well as contextual variables related to motion, task engagement, behavioral state, rewards, punishment, and novelty or familiarity of the environment (Ainge et al., 2007; Danielson et al., 2016; Fenton et al., 2010; Frank et al., 2000; Hollup et al., 2001; Leutgeb et al., 2005; Markus et al., 1995; Monaco et al., 2014; Muller and Kubie, 1987; Pastalkova et al., 2008; Ranck, 1973; Smith and Mizumori, 2006; Wood et al., 1999; Wood et al., 2000). Such observations reinforce the notion that ensembles of hippocampal neurons constitute a complex cognitive map of experience (O'Keefe and Nadel, 1978).

As these contextual variables change, the firing of individual neurons comes and goes at various timescales (flexibility) while preserving the ability to represent critical features reliably (robustness) with sparse population activity (Olshausen and Field, 2004; Rich et al., 2014; Treves and Rolls, 1994; Tsodyks and Feigel'man, 1988; Ziv et al., 2013). As experiences unfold, environments change, and learning proceeds, neurons need to be recruited to or released from the active ensembles for different representations at approximately equal rates. Thus, each neuron should be capable of reversibly and efficiently switching between active and inactive states, as has been observed (e.g., Frank et al., 2004; Leutgeb et al., 2005; Markus et al., 1995; Ziv et al., 2013).

The output of the pyramidal neurons is determined by the properties of the synaptic inputs they receive as well as their excitability. For example, regulation of cellular membrane potential is an efficient and reversible mechanism that may allow spatially tuned neuronal firing to be modulated by context or network-wide adaptive control. Indeed, a recent study (Lee et al., 2012) demonstrated that changes of membrane potential have striking effects on spatially modulated activity. Using whole-cell patch-clamp recording in hippocampal area CA1 of awake, freely moving rats, Lee et al. found that a small, constant depolarization of somatic membrane potential (V_m) by just a few millivolts could rapidly and reversibly convert a pyramidal neuron from a silent cell (i.e., without place-related firing) to a place cell; conversely, a small hyperpolarization could convert the neuron function from a place cell to a silent cell. Remarkably, this rapid, V_m-dependent creation or removal of place-cell firing was accompanied by a strikingly nonlinear voltage dependence of spatially tuned synaptic responses recorded below action potential threshold.

To determine what kinds of cellular mechanisms support this steep voltage dependence of spatially modulated synaptic responses, we used a pharmacological approach while performing patch-clamp recording from CA1 pyramidal neurons in brain slices (*in vitro*) and in awake, behaving mice during navigation of virtual environments (*in vivo*). Our experiments revealed a critical contribution of persistent sodium current, which mediated high-gain, subthreshold synaptic amplification, consequently driving spatially dependent firing in CA1 pyramidal neurons. In addition, motivated by a recent finding that dendritic plateau potentials can induce the formation of new, long-lasting place fields in pyramidal neurons via synaptic plasticity (Bittner et al., 2015; Bittner et al., 2017), we found that dendritic plateau potentials were facilitated by dendritic depolarization. Therefore, we propose that multiple voltage-dependent mechanisms can influence place-cell firing: depolarization contributes to the conjunctive responses of hippocampal neurons to inputs carrying information about place and other contextual features, as well as the formation and/or stabilization of these neural representations via synaptic plasticity.

Results

Steep voltage dependence of synaptic responses in vitro

To study the cellular mechanisms underlying the steep dependence of synaptic responses on baseline V_m observed *in vivo* (Lee et al. 2012), we first sought to reproduce this phenomenon *in vitro*. Somatic whole-cell patch-clamp recordings were obtained from CA1 pyramidal neurons in acute hippocampal slices, and stimulating electrodes were used to activate synaptic inputs from the entorhinal cortex (EC) onto the distal apical tuft dendrites and/or from CA3 onto more proximal dendrites. GABAergic inhibition was blocked in order to isolate excitatory synaptic responses (unless noted otherwise).

We mimicked the property of silent cells observed *in vivo* (Lee et al., 2012), which had little observable spatially tuned somatic responses, by stimulating synapses *in vitro* at low intensities to produce small, subthreshold excitatory postsynaptic responses (EPSPs) at or near the resting V_m (average peak response < 2.5 mV for one-pathway stimulation and < 5 mV for two-pathway stimulation, for all stimulus patterns tested; see below). To examine the voltage dependence of these responses, we applied *DC* current injection via the somatic patch electrode to modulate baseline V_m, again mirroring previous experiments (Lee et al., 2012).

In this experimental design, we regard activation of EC and/or CA3 inputs as corresponding to transient, spatially modulated synaptic inputs. We view the constant current injection as a counterpart of relatively slow synaptic responses, which might convey contextual information or drive an adaptive control of network activity level.

For low-frequency activation of EC synapses, temporally isolated EPSPs had a shallow voltage dependence (Figure 1A). In contrast, for high-frequency activation of EC synapses, burst EPSPs showed a strikingly steep voltage dependence, with the steepest transition occurring within a narrow range of ~4 mV, centered around −56 to −57 mV (Figure 1B; for peak amplitude, −56.4±0.8 mV, for integral, −57.0±0.7 mV, n=6 neurons from 5 rats), and an amplification ratio of 3–5 fold (for peak amplitude, 3.06±0.16, for integral, 4.78±0.28, n=50 neurons from 41 rats). All of these measures were nearly identical to the values reported *in vivo* (Lee et al., 2012). Notably, even very small temporally summated EPSPs (average peak response < 1 mV near the resting V_m) manifested this voltage-dependent amplification (see the example in Figure 1B); however, temporally isolated EPSPs with matched or even larger peak amplitudes did not (compare the examples in Figure 1A and 1B). The voltage-dependent synaptic amplification was robust across cells (50/50 neurons tested).

As in Lee et al. (2012), we observed a steep transition of responses at V_m below the threshold for somatic action potential firing. For a given cell, amplified EPSPs at V_m beyond the transition V_m (defined as the baseline V_m for which the difference between all of the responses at more hyperpolarized versus more depolarized V_m was maximized, see STAR Methods) were usually large enough to trigger action potentials, as observed *in vivo*. Importantly, although action potentials are known to activate many different membrane currents (Anwyl, 1999; Bean, 2007; Magee and Carruth, 1999; Park et al., 2010), synaptic amplification was observed prior to the first action potential in every cell tested (e.g., Figure 1B,C). Moreover, after a spike removal procedure was applied (see STAR Methods), the peak depolarization measured always occurred just prior to the initiation of the first action potential. Therefore, voltage-dependent amplification can promote action potential firing, but does not require it.

To test the robustness of the synaptic amplification *in vitro*, we assessed the influences of some factors that differ between *in-vitro* and *in-vivo* conditions. First, although synaptic inhibition was blocked in the experiments described so far, we also observed synaptic amplification when GABAergic inhibition was intact (Figure S1A). Second, in exploring animals, CA1 pyramidal neurons receive excitatory inputs from multiple synaptic pathways. We showed that the amplification *in vitro* was observed when either one or both major excitatory pathways were stimulated (see below). Third, the activity of hippocampal neurons *in vivo* is modulated by strong theta rhythm when the animal is exploring an environment. The amplification was the same when synaptic activation was performed using bursts of high-frequency stimulation modulated at a theta frequency (5 Hz, i.e., inter-burst interval of 200 ms; Figure S1B; for both peak amplitude and integral, $p > 0.05$ by Student's t-test).

CA1 pyramidal neurons show prolonged and time-varying activity *in vivo* when an animal traverses a place field (Harvey et al., 2009; Lee et al., 2012; O'Keefe, 1976), as do upstream neurons which provide the synaptic input they receive (Domnisoru et al., 2013; Schmidt-Hieber and Häusser, 2013). To determine whether the synaptic amplification *in vitro* generalizes to behaviorally relevant timescales and dynamics, we used a stimulus pattern of a longer total duration (1.2 seconds) and the instantaneous frequency modulated by a slow, symmetric ramp (minimum ~3 Hz, maximum ~50 Hz). For this ramp-modulated activation of EC synapses, EPSPs also showed a robust, steep voltage dependence (9/9 neurons from 9 rats; Figure 1C), which was observed across different combinations of total duration and frequency range tested as long as EPSPs exhibited temporal summation (additional parameters tested: 2.2, 4 seconds for duration; 12, 20, 100, 150 Hz for maximum instantaneous frequency; apparent amplification observed at 100 and 150 Hz; data not shown, n=4 neurons from 4 rats).

These experiments demonstrate that the steep dependence of synaptic responses on V_m observed *in vivo* can be recapitulated using a reduced, *in-vitro* system. Even very small synaptic responses (< 1 mV measured near the resting V_m) that persisted for behaviorally relevant timescales (seconds) exhibited voltage-dependent amplification with a high gain upon somatic depolarization. The ability to recapture these features *in vitro* facilitates detailed mechanistic analyses.

Pharmacological profile of the steeply voltage-dependent amplification in vitro

To determine which kinds of voltage-dependent ion channels underlie the amplification of synaptic responses, we applied various pharmacological agents via the bath. Surprisingly, we found that blocking *N*-methyl-D-aspartate receptor (NMDAR; with 50 µM AP5, Figure 2A) or L-, T-, and R-type voltage-gated calcium (Ca_v; with 50 µM Ni^{2+} and 10 µM nimodipine, Figure 2B) channels had only marginal effects on the synaptic amplification. In contrast, partial block of voltage-gated sodium (Na_v) channels by a relatively low (20 nM) concentration of tetrodotoxin (TTX) greatly reduced the amplification in response to activation of EC or CA3 input, alone or together (Figure 2C, D, S2A). We also tested the effects of phenytoin, another Na_v channel blocker with a higher selectivity for the sustained component of sodium current (Kuo and Bean, 1994; Segal and Douglas, 1997). Using a moderately low concentration (100 µM) to reduce nonspecific effects (Castro-Alamancos et al., 2007; Chao and Alzheimer, 1995; Segal and Douglas, 1997; Su et al., 2001), we found that partial block of Na_v channels by phenytoin significantly reduced the amplification (Figure S2B). These results indicate that a current mediated by Na_v channels critically contributes to the amplification of synaptic responses.

Consistent with previous work showing that low TTX had presynaptic effects during weak synaptic stimulation (Kim et al., 2015), we observed a reduction (presumably presynaptic) of responses in low TTX for cells with relatively small baseline EPSPs (average peak response < 1.6 mV in control, reduced to 39% of control, n=3 neurons from 3 rats, and reduced to noise level for 2 additional neurons from 2 rats), but not for cells with larger baseline EPSPs (average peak response > 1.6 mV in control, 108% of control, n=2 neurons from 2 rats). Nevertheless, we attribute the strong effects of low TTX on synaptic amplification to a postsynaptic action (for a total of 5 neurons with identifiable EPSPs remaining in low TTX), for the following reasons. First, as discussed above, even very small synaptic responses (< 0.5 mV at or near the resting V_m; e.g., Figure 1B) exhibit steeply voltage-dependent amplification. Although burst EPSPs were on average smaller in low TTX (average peak amplitude=1.19 ± 0.48 mV, 66% of control, n=5 neurons), these responses were similar to (or larger than) those from a subset of cells with relatively small baseline EPSPs in control (< 1.19 mV, n=8 neurons from 6 rats, average peak amplitude=0.92±0.08 mV), which were capable of strong synaptic amplification in the absence of TTX (amplification ratio: peak amplitude, 3.34±0.52, integral, 5.49±1.19). This argues against a role of reduced response size in the effects of TTX on the voltage-dependent amplification. Second, the block of amplification by low TTX was very similar when comparing cells with no reduction of baseline EPSPs (108% of control; amplification ratio in low TTX: peak amplitude, 1.05±0.03, integral, 1.40±0.02) and cells with a reduction of baseline EPSPs (39% of control, owing to the presynaptic effect; amplification ratio in low TTX: peak amplitude, 1.18±0.21, integral, 1.72±0.51).

To further test whether the effective block of synaptic amplification by low TTX is indeed a postsynaptic rather than a presynaptic effect, we performed experiments with a low concentration of an intracellular Na_V channel blocker QX-314 (0.5 mM, in the patch pipette). This concentration—approximately one order of magnitude lower than what is typically used (e.g., Palmer et al., 2014; Stuart and Sakmann, 1994)—was chosen to minimize confounding off-target effects, yet it completely blocked synaptic amplification (Figure 3A). Furthermore, we found that intracellular low QX-314 abolished the non-inactivating component of the sodium current isolated in somatic whole-cell voltage-clamp recordings (Figure 3B–D), without completely blocking the large transient component in response to a voltage step to 0 mV (data not shown, see STAR Methods for details). Together, these data indicate that a postsynaptic voltage-gated sodium current is crucial for the steeply voltage-dependent amplification of temporally summated synaptic responses in CA1 pyramidal neurons (Figure 2E), and that the sustained or persistent component may play a particularly important role. Although QX-314 is known to have off-target effects, the low concentration we used may reduce this concern; the consistency between the results of TTX and QX-314 makes block of Na_V channels the parsimonious interpretation. Finally, we performed other experiments to eliminate alternative possibilities (Figure 2, and see below).

Cellular localization of the steeply voltage-dependent amplification in vitro

We combined a few experimental approaches to determine the cellular location of the synaptic amplification. First, instead of electrically stimulating afferent axonal fibers, which should synaptically activate channel conductances along the somato-dendritic axis, we simulated the arrival of synaptic current at the soma by injecting synaptic current-like waveforms via the patch electrode (“simulated EPSPs”). Second, we patched either the soma or the distal primary apical dendrite to compare amplification at different locations. Third, we activated synapses from different input pathways, which impinge upon different dendritic compartments.

When synaptic responses were simulated in the perisomatic region by current injection, voltage-dependent amplification for simulated burst EPSPs and ramp EPSPs was robust across cells (for burst with inhibition blocked, 55/55 neurons from 47 rats; for ramp with inhibition blocked, 13/13 neurons from 12 rats; for ramp with inhibition intact, 5/5 neurons from 5 rats). The amplification of simulated responses was not significantly different from the amplification of synaptically activated responses, regardless of whether GABAergic inhibition was blocked or not (Figure 4A–D, S1A; $p > 0.05$ by one-way or two-way ANOVA, for all comparisons). Together with the experiment using low QX-314 (Figure 3A), these results support a postsynaptic amplification mechanism. Furthermore, because voltage strongly attenuates along the dendrites of CA1 pyramidal neurons (Golding et al., 2005), thus limiting the spatial spread of somatically simulated EPSPs into the dendrites, these experiments suggest that a perisomatic mechanism is sufficient to produce the steeply voltage-dependent amplification of synaptic responses.

To compare the amplification locally in the dendrites with the amplification observed at the soma, we performed recordings from the distal apical dendritic trunk (198–356 m, 266±25 m from the soma, ~50–90% of the distance from the soma to the end of the apical tuft; n=7 neurons from 7 rats). To mimic the conditions of the somatic recording experiments, we compensated for the attenuation of EPSPs (distal dendrite→soma) and the attenuation of steady-state V_m modulation (soma→distal dendrite), both of which are ~50% (for distal dendrites 200–350 m from the soma, Golding et al., 2005): first, compared to the somatic recordings, stimulus was adjusted to yield ~2-fold larger EPSPs at or near the resting V_m (average peak response < 5 mV for one-pathway stimulation and < 10 mV for two-pathway stimulation); second, *DC* current injection was applied via the dendritic patch electrode (series resistance=11–35 M) to modulate V_m over about half of the range tested in the somatic recordings.

We found that amplification observed in the distal dendrite (Figure 4E, F, S3A) was much smaller than amplification observed at the soma (Figure 2D, S2A, 4C,D; for both peak amplitude and integral, $p < 10^{-7}$ by two-way ANOVA with *post-hoc* means comparison using Tukey's test). Relatively little dendritic amplification was reproduced when responses were simulated using synaptic current-like waveforms injected via the dendritic patch electrode (Figure 4E,F; for both peak amplitude and integral, $p > 0.05$ by two-way ANOVA). These results suggest that dendritic conductances contribute only minimally to synaptic amplification in response to modulation of perisomatic V_m.

Taken together, these experiments suggest that the steeply voltage-dependent amplification of temporally summated synaptic responses observed at the soma is mediated primarily by a perisomatic voltage-dependent mechanism.

This hypothesis predicts that the amplification would depend mainly on the size of somatic EPSPs and the perisomatic V_m, and therefore should be similar even when synaptic responses originate from different dendritic locations. We compared amplification in response to different combinations of inputs, and found it was indeed the case, regardless of whether it was measured from the soma (Figure 2D, S2A, 4C,D) or from the dendrite (Figure 4E,F, S3A; for both peak amplitude and integral, $p > 0.05$ by two-way ANOVA). Furthermore, if the amplification of synaptically activated responses is mediated primarily by the same mechanism that mediates the amplification of somatically simulated responses, they should share the same pharmacological profile. Indeed, this was true (Figure S3B–H; for pharmacological effects on both peak amplitude and integral, $p > 0.05$ by two-way ANOVA), and the hypothesis was further supported by a complete block of perisomatic amplification using a higher concentration of TTX (1 μM, Figure S3E). These results support the notion that a perisomatic, voltage-gated sodium current is sufficient and critical for the synaptic amplification.

We also assessed the effects of additional candidate mechanisms with strong subthreshold voltage sensitivity on the amplification. We found that partial block of A-type voltage-gated potassium (K_v) channels and G-protein-coupled inwardly-rectifying K_v channels (with 150 μM Ba^{2+}) or hyperpolarization-activated and cyclic-nucleotide-gated (HCN) channels (with 5 or 10 μM ZD7288) did not significantly change the synaptic amplification of simulated EPSPs (even when assessed at less depolarized V_m during block of K_v or HCN channels to avoid continuous, runaway firing; see STAR Methods for details of experimental design; Figure S3I,J). Furthermore, subsequent application of TTX (1 μM) completely eliminated the amplification observed in the presence of the blocker (Figure S3I,J). Therefore, by rejecting other hypotheses, these results further support the conclusion that the synaptic amplification is driven by Na_v channels.

Persistent sodium current mediates steeply voltage-dependent amplification in silico

The evidence described so far suggested that a perisomatic, subthreshold voltage-gated sodium current is the critical mechanism underlying the steeply voltage-dependence synaptic amplification *in vitro*. Although transient, subthreshold sodium current can be activated by single EPSPs in CA1 pyramidal neurons (Carter et al., 2012), we found that temporally isolated EPSPs exhibited little synaptic amplification (Figure 1A). Furthermore, the transient current nearly fully inactivates within the period of a single EPSP (Carter et al., 2012), and thus is expected to remain inactive during amplification of temporally summated responses (Figure 1B, C). This suggests that a non-inactivating (“persistent”) sodium current is responsible for the synaptic amplification we observed. The origin of persistent sodium current in CA1 pyramidal neurons is quantitatively well explained by the steady-state current from Na_v channels expressed at high density in the proximal axon that drive action potential firing; there is no need for channels with special biophysical properties (Carter et al., 2012).

If this is correct, then computational simulations using realistic models of conventional Na_v channels should naturally reproduce the steeply voltage-dependent synaptic amplification observed in our experiments. We tested this using two computational models.

We first tested whether Na_v channels with properties found in CA1 pyramidal neurons are sufficient to support synaptic amplification using a single-compartment model with a leak conductance and a Na_v-channel conductance modeled by the Markovian dynamics described in Carter et al. (2012). When the Na_v-channel conductance was adjusted to reflect the amount of persistent sodium current observed near the soma of CA1 pyramidal neurons (Carter et al., 2012), and without any further tuning of the Na_v-channel model, we reproduced the subthreshold amplification observed in our experiments, which was mediated by a subthreshold sodium current (Figure 5A, S4A). In addition, as expected from theoretical considerations (Carter et al., 2012; Taddese and Bean, 2002; see Discussion), persistent sodium current and synaptic amplification were also observed using Hodgkin-Huxley models of Na_v channels (data not shown, see STAR Methods).

To determine how much of the synaptic amplification observed in the model is explained by persistent sodium current, we assessed activation of transient and persistent sodium current by simulating voltage-clamp experiments using the burst EPSP as the voltage command (Figure 5A), with the baseline V_m set to a value where synaptic responses were strongly amplified. Total and persistent (i.e., nearly steady-state) sodium current were defined by comparing the responses to the real-time EPSP and a 50X slower waveform. The two currents were nearly identical (Figure 5B, *top-left*), suggesting that the subthreshold, persistent sodium current is sufficient to support the amplification. However, when the baseline V_m was pushed to more depolarized levels, a small transient current was observed (i.e., the difference between the total and the persistent current; Figure 5B, *bottom-left*, at V_m above the spike threshold of the model); this was more pronounced for a single, amplitude-matched EPSP (Figure 5B, *right*). These results demonstrate that engagement of transient sodium current depends on both the membrane potential and the kinetics of synaptic responses. Under the conditions where subthreshold amplification occurs, the persistent component of the sodium current is the primary contributor.

If the synaptic amplification is primarily mediated by persistent sodium current which naturally emerges as a consequence of activation of the same Na_v channels that drive action potentials, existing models of CA1 pyramidal neurons with only a standard type of axonal Na_v channels should recapitulate these phenomena. To test this, we used a previously described, detailed model of CA1 place cells that was constrained by published data (Grienberger et al., 2017, see STAR Methods). Without any tuning of this model to fit our data, the simulations using subthreshold EPSPs reproduced almost all of the characteristic features observed in the synaptic amplification *in vitro*, including steep subthreshold voltage sensitivity (the steepest transition at −56 to −58 mV), a much higher dependence on Na_v channels than NMDAR, A-type K_v and HCN channels, perisomatic localization, and stronger effects on the later phase of a temporally summated response (Figure 5C_1, S4B,C, S5A_1,B). By examining voltage and ionic currents in different cellular compartments (Figure 5C_1-C_3, S4B,C, S5), the results indicated that these characteristics were mostly explained by the presence of a high conductance of the Na_v channels in the axonal initial segment, as well as the strong voltage attenuation along the dendrites. In addition, the axonal Na_v channels were activated at more hyperpolarized V_m than dendritic NMDAR channels (see also Carter et al., 2012; Spruston et al., 1995) and dendritic Na_v channels (see also Colbert and Pan, 2002; Gasparini and Magee, 2002; Hu et al., 2009; Magee and Johnston, 1995; Royeck et al., 2008).

Thus, the computational modeling independently support our experimental results, further suggesting that the subthreshold, perisomatic persistent sodium current is both sufficient and necessary for steeply voltage-dependent synaptic amplification.

To further explore the functional consequences of voltage-dependent amplification on synaptic integration, we simulated temporally summated responses with varying levels of synaptic input and determined the contribution made by persistent sodium current. In both the simple and detailed models, persistent sodium current greatly reduced the synaptic conductance required to reach action potential threshold (defined in the condition with Na_V channels), both at the resting V_m of the models (reduced by 54% in the simple model and 37% in the full model) or upon steady depolarization of V_m by 5 mV (reduced by 74% in the simple model and 44% in the full model; Figure 6). Furthermore, persistent sodium current allowed inputs to be further amplified upon steady depolarization (Figure 6).

Even without the subthreshold nonlinearity, spatially tuned input could still drive neuron firing upon a small depolarization of just a few millivolts; in this case, however, the synaptic inputs would have to be generally stronger (Figure S6). The possible advantages of maintaining spatially tuned synaptic inputs in a relatively weak state, while allowing them to be amplified or potentiated under certain conditions, are considered in the Discussion.

Voltage-dependent amplification of synaptic responses in vivo

Based on our *in-vitro* experiments and computational models, we posit that persistent sodium current critically contributes to the steep voltage dependence of spatially tuned synaptic responses *in vivo*. To test this hypothesis, we performed somatic whole-cell recordings from CA1 pyramidal neurons of the dorsal hippocampus in mice trained to navigate simulated visual environments (see STAR Methods; Cohen et al., 2017). Animals ran unidirectionally along oval-shaped tracks (150 cm-long, 12 cm-wide) with salient proximal and distal visual cues, as well as water rewards delivered at two fixed locations.

We examined the voltage dependence of spatially dependent synaptic responses *in vivo*. Recordings of pyramidal neurons were identified based on stereotaxic location and firing pattern, which typically included complex spikes (high-frequency burst with decreasing spike amplitudes). During running, V_m below action potential threshold exhibited prominent theta-frequency modulation (Figure S7C) and prolonged, ramp-like position-dependent responses (observed in 6/7 neurons from 7 mice, see STAR Methods), regardless of whether or not the neuron exhibited place-dependent action potential firing. Upon modulation of V_m by injecting *DC* current to the soma, these spatially modulated synaptic ramps showed a strong voltage dependence (Figure 7A,C). At relatively depolarized V_m, amplified ramps were always large enough to drive somatic action potentials, resulting in spatially dependent firing activity, consistent with what was observed in similar experiments performed by Lee et al. (2012).

Voltage-dependent synaptic amplification in vivo is supported by persistent sodium current

A number of observations from the *in-vivo* experiments are consistent with our mechanistic model that subthreshold persistent sodium current is responsible for the voltage-dependent amplification of spatially modulated synaptic responses, which drives strong voltage sensitivity of place-dependent neuron output.

The synaptic amplification observed *in vitro* either did not change the temporal profile of synaptic responses at all (e.g., Figure 1C) or only modestly (at a timescale of tens of milliseconds) in certain circumstances (e.g., Figure 1B). This is consistent with the rapid activation and deactivation kinetics as well as the non-inactivating property of persistent sodium current (Carter et al., 2012). At the running speeds of the mice in our experiments (typically 10–30 cm/s; range=3–60 cm/s), this level of temporal mismatch should correspond to very small spatial differences for responses at different V_m. In keeping with this prediction, we observed a strong coherence between the spatial profiles of V_m below action potential threshold at different somatic V_m (Figure S7A). Thus, synaptic amplification *in vivo* has a property consistent with the biophysics of the persistent sodium current.

Our mechanistic model also suggested that the synaptic amplification occurs independently of somatic action potential firing. This was indeed the case *in vivo*, as indicated by the following two observations:

1. For 3/7 neurons (from 7 mice) with small spatially modulated responses at relatively hyperpolarized V_m, the *DC* current injection was not expected to be large enough to allow the peak responses to cross the lowest apparent voltage threshold for action potential firing. However, amplification of subthreshold synaptic responses still occurred in these cells, which drove firing at depolarized V_m (Figure S7B), suggesting that the amplification does not require action potentials.
2. For 2/7 neurons (from 7 mice), the initial portion (in space) of some amplified, spatially modulated ramps (i.e., at relatively depolarized V_m) was not large enough to drive action potential firing at all or only to a very limited extent (0.48±0.36 spikes/lap in the initial portion, 4 spatially modulated ramps; Figure S7D). In addition, these ramps arose following an extended period of quiescence (~3–10 seconds) when there was minimal firing or none, so the contribution of slow, spike-driven currents from action potentials to the observed amplification is likely to be negligible.

Taken together, these observations suggest that synaptic amplification of spatial responses is not attributable to action potential firing at the soma; rather, it is mediated by a mechanism with strong subthreshold activation.

To directly test whether the voltage-dependent amplification of spatially modulated synaptic responses is driven by persistent sodium current, we blocked it in the recorded cell *in vivo* using the low concentration (0.5 mM) of intracellular QX-314, which produced robust effects on synaptic amplification *in vitro*, attributable to partial block of Na_v channels (Figure 2, 3, S3). In the *in-vivo* recordings, as QX-314 dialyzed into the cell, significant time- and activity-dependent reduction of firing was observed, without obvious signs of off-target and network-wide actions (see STAR Methods for more details; Figure S7C).

We found that low QX-314 significantly reduced the voltage-dependent amplification of spatially dependent synaptic ramps *in vivo* (n=6 neurons from 6 mice; Figure 7B,C), presumably through block of persistent sodium current. However, an alternative interpretation should be considered. Low QX-314 reduces action potential firing and hence spike-driven currents, which could also mediate the observed amplification. The observation that the amplification did not require somatic action potentials argues against this possibility (Figure S7B,D). Furthermore, we compared the voltage dependence of the initial portion of spatially modulated synaptic ramps following an extended period of quiescence, identified as described above. In contrast to the recordings under the normal condition, with intracellular low QX-314, we found that the initial, relatively quiescent portion of these spatially modulated ramps was not apparently voltage-dependent (3/3 neurons from 3 mice; 3 spatially modulated ramps selected with matched, limited firing as the normal cases, 1.10±1.57 spikes/lap in the initial portion; Figure S7D). These observations suggest that intracellular low QX-314 reduces the voltage dependence of synaptic responses by blocking subthreshold persistent sodium current rather than by inhibiting action potential firing.

In summary, all of these lines of evidence suggest that persistent sodium current critically contributes to the voltage dependence of spatial coding in CA1 pyramidal neurons *in vivo*, by mediating voltage-dependent amplification of spatially tuned synaptic responses, even at membrane potentials below somatic action potential threshold.

Additional voltage-dependent mechanisms may contribute to spatially modulated firing of hippocampal pyramidal neurons

Perisomatic persistent sodium current might not be the only form of synaptic amplification relevant for place-cell firing. The *in-vitro* experiments and computational simulations described above involved only relatively small synaptic responses and mild steady depolarization of the soma. When synaptic inputs are stronger, they generate large, transient depolarization in the dendrites, which may also engage dendritic Na_v channels. To test this idea *in vitro*, we took advantage of the observation that the presynaptic effects of low TTX on synaptic transmission are negligible for relatively strong synaptic stimulation (Kim et al., 2015). We analyzed the effects of low TTX on responses to relatively high stimulus intensities (but still subthreshold), without any steady modulation of somatic V_m (baseline V_m held near −65 mV). Partial block of Na_v channels by low TTX had minimal effects on burst EPSPs evoked using the lowest intensities tested (Figure S8A,B), consistent with previous results. However, low TTX inhibited larger burst EPSPs (Figure S8A,B), suggesting that postsynaptic Na_v channels are significantly recruited by stronger transient depolarization. We also performed experiments with subthreshold synaptic responses simulated using somatic current injection. We found that for larger responses, the effects of low TTX on simulated burst EPSPs were smaller than the effects on synaptically activated EPSPs (Figure S8A,B); this difference was on the threshold of statistical significance (for the slope of amplitude relationship between control vs. low TTX, $p = 0.05$ by Student's paired t-test). Because the spatial spread of simulated responses is expected to be relatively restricted to the perisomatic region (Golding et al., 2005), the stronger effects of low TTX on synaptically activated EPSPs suggest that in addition to perisomatic Na_v channels, larger synaptic responses activate dendritic Na_v channels to some degree. Together, these results demonstrate that activation of two amplification mechanisms—mediated by perisomatic and dendritic Na_v channels via persistent sodium current—can both be promoted by transient depolarization resulting from relatively strong synaptic inputs. While the high density of axonal Na_v channels allows them to contribute to synaptic amplification in response to relatively weak inputs, the lower density of dendritic Na_v channels (Lorincz and Nusser, 2010) limits their contribution to circumstances involving stronger synaptic responses.

At even stronger levels of synaptic activation and dendritic depolarization, dendritic ion channels can produce regenerative dendritic events (Major et al., 2013; Stuart et al., 2016; Stuart and Spruston, 2015), which can induce robust, long-lasting synaptic plasticity (Kim et al., 2015; Remy and Spruston, 2007; Takahashi and Magee, 2009). One type of such events, called dendritic plateau potentials, driven by NMDAR and Ca_v channels and promoted by backpropagating action potentials, has been shown to produce new place fields in CA1 pyramidal neurons (Bittner et al., 2015) via potentiation of synaptic input (Bittner et al., 2017). We examined the effects of steady dendritic depolarization or strong synaptic stimulation on synaptic responses using recordings from the distal primary apical dendrite *in vitro* (198–356 m, 266±25 m from the soma). With relatively weak synaptic stimulation and mild modulation of dendritic V_m (Figure 4E,F, S3A), there was no indication of plateau potentials in the dendritic recordings. However, we found that stronger synaptic activation or larger steady dendritic depolarization facilitated the occurrence of dendritic plateau potentials (Figure 8). Synaptic inputs were necessary for dendritic plateau potentials observed at depolarized dendritic V_m, as they did not occur when EPSPs were simulated using current injection (no plateau potential observed in 7 neurons from 7 rats; Figure S8C), consistent with the critical role of glutamate release and NMDAR activation for the generation of plateau potentials.

Thus, we present evidence for multiple synaptic amplification mechanisms, which exist in different cellular compartments and are mediated by different ion channels. All of these mechanisms can, in principle, contribute to the voltage dependence of spatially modulated responses and firing in hippocampal pyramidal neurons.

Discussion

Hippocampal pyramidal neurons that lack spatially dependent spiking output nevertheless receive spatially tuned synaptic inputs, which can be revealed by a change of baseline membrane potential as little as a few millivolts (Lee et al. 2012). Here, we show that this rapid and reversible conversion between silent cells and place cells is driven by voltage-dependent amplification of spatially modulated synaptic responses via a voltage-gated sodium current operating in a mode consistent with “persistent sodium current” (French et al., 1990; Crill, 1996). Our results add to the list of contributions made by Na_v channels to neuronal function on timescales across several orders of magnitude (Branco et al., 2016; Colbert and Pan, 2002; Golding and Spruston, 1998; Hu et al., 2002; Kim et al., 2015; Kole et al., 2008; Park et al., 2013; Stuart and Sakmann, 1995; Stuart et al., 1997; Yamada-Hanff and Bean, 2013).

The quantitative consistency of the transition voltage values observed here and in Lee et al. (2012) suggests that persistent sodium current plays a critical role for the hyperpolarized voltage sensitivity observed in both studies. Although we did see spatially modulated responses at relatively hyperpolarized V_m—consistent with another study using similar head-fixed virtual reality for mice (Cohen et al., 2017)—Lee et al. generally did not. Differences in the experimental conditions (head-fixed mice here versus freely moving rats in Lee et al.) and prior exposure to the recording environments (i.e., familiar here versus novel in Lee et al.) most likely explain the difference in this aspect of the results. Small fluctuations in V_m—difficult to be detected as clear spatial tuning in the *in-vivo* recordings —could nevertheless be amplified by persistent sodium current at more depolarized V_m. Alternatively, additional mechanisms may work together with persistent sodium current to contribute to the voltage-dependent place-cell firing in freely moving rats (Lee et al., 2012), nevertheless resulting in voltage dependence identical to that observed in our experiments.

Cellular and biophysical mechanisms

The steeply voltage-dependent amplification can be explained by the cellular and biophysical characteristics of persistent sodium current in CA1 pyramidal neurons. These include subthreshold half-activation voltage (−62 mV with liquid junction potential corrected), rapid activation and deactivation, little or no inactivation, and localization near the soma (Carter et al., 2012). The positive feedback nature of persistent sodium current, as well as the high density of axonal Na_v channels (Carter et al., 2012; Kole et al., 2008; Lorincz and Nusser, 2010), mediate the steepness of the voltage dependence of synaptic amplification, while the lack of inactivation favors amplification of temporally summated synaptic responses during spatial navigation.

Subthreshold persistent sodium current can be generated by an equilibrium between the activation and incomplete inactivation of Na_v channels; thus, the persistent and transient components of sodium current can arise from the same channels that drive action potentials (Taddese and Bean, 2002; Carter et al., 2012). Our models suggest that the high conductance of a single type of Na_v channels in the axon initial segment is sufficient to produce the subthreshold nonlinearity of synaptic responses. Multiple subtypes of Na_v channels can contribute to the persistent sodium current, as both $Na_v1.6$ and $Na_v1.2$ are expressed in the axon initial segment of CA1 pyramidal neurons (Hu et al., 2009; Lorincz and Nusser, 2010). Each type mediates both transient and persistent current, although $Na_v1.6$ may contribute more, as it activates at slightly more hyperpolarized V_m (Hu et al., 2009; Royeck et al., 2008).

Our results demonstrate that dendrites can contribute to voltage-dependent amplification in response to strong dendritic depolarization via multiple mechanisms (Figure 8, S8), which likely involve Na_v and Ca_v channels, as well as NMDARs (Larkum et al., 1999; Schiller et al., 1997; Takahashi and Magee, 2009).

Identifying the physiological sources of V_m modulation will require more investigation. *In vivo*, CA1 place cells have a baseline V_m more depolarized than the critical voltage for subthreshold amplification (−57 mV), while silent cells are more hyperpolarized (Cohen et al., 2017). Furthermore, conversion of cell identity sometimes resulted from spontaneous, natural changes in V_m (Lee et al., 2012). Glutamate and GABA are likely candidates for mediating cell-specific depolarization and hyperpolarization, respectively (e.g., Grienberger et al., 2017). These transmitters and others may also mediate broader, network-wide effects (Cobb and Lawrence, 2010; Hasselmo and Giocomo, 2006). For example, subcortical projections to the hippocampus from the medial septum contain glutamatergic, GABAergic, and cholinergic inputs (Colom et al., 2005; Freund and Antal, 1988; Leranth and Frotscher, 1987; Teles-Grilo Ruivo and Mellor, 2013), which are modulated by behavioral variables such as running speed (Fuhrmann et al., 2015). Thus, a variety of neurotransmitter systems could modulate place-cell activity in the hippocampus by regulating V_m through multiple cellular mechanisms.

Implications of multiple mechanisms for adaptive spatial coding by hippocampal pyramidal neurons

While coincidence detection of spatially modulated input and other (contextual) input could, in principle, be mediated by linear summation, the existence of subthreshold nonlinear amplification confers some functional advantages. Without synaptic amplification, spatially modulated inputs would need to be stronger (Figure 6). As a result, neuronal output would be more sensitive to variability in the input. If the coincidence detection is a desired feature of place-cell firing, this would be harder to ensure with strong spatially modulated inputs, especially if noise were related to the size of synaptic responses (as in Figure S6). Synaptic amplification minimizes this problem, and in doing so promotes a requirement for coincidence of multiple, weaker inputs conveying different kinds of information to drive action potentials. Furthermore, with weak inputs requiring amplification, excessive firing might be avoided, thus promoting sparsity and enhancing the flexibility and robustness of the hippocampal code.

While our results and Lee et al. (2012) suggest that place-cell firing can be induced by small somatic depolarization, other studies suggests that it can be created by large, transient dendritic plateau potentials that drive synaptic plasticity (Takahashi and Magee, 2009; Bittner et al., 2015; Bittner et al., 2017). Both mechanisms could be relevant *in vivo*. Place-cell firing produced by synaptic amplification is rapidly reversible, whereas dendritic plateau potentials would likely create temporally stable place fields in CA1 pyramidal neurons.

While the role of synaptic plasticity in shaping hippocampal representations during learning has been considered extensively (O'Keefe and Nadel, 1978; Shapiro and Eichenbaum, 1999), the function of the more transient modulation of place-cell activity by small changes in V_m is less apparent. We speculate that synaptic amplification could contribute to the hippocampal map in at least two ways.

First, this mechanism might facilitate the conjunctive coding of multiple features in the hippocampal map. The dynamic readout of this map reflects not only the changing position of an animal, but also associated information about other motion- or task-related behavioral variables (e.g., Smith and Mizumori, 2006; Wood et al., 1999; Ainge et al. 2007). For example, inputs from midline thalamic nucleus reuniens carrying trajectory-related information (Ito et al., 2015) could modulate V_m to engage the subthreshold nonlinearity and support trajectory-dependent place-cell firing.

Second, synaptic amplification could promote adaptive, network-wide regulation of place-cell firing. For instance, upon introduction of an animal to a new environment, neuromodulatory inputs could mediate concerted depolarization or hyperpolarization of many cells, which would modify the active fraction of pyramidal neurons in the network. Thus, by exploiting the high-sensitivity and reversibility of the voltage-dependent synaptic amplification, hippocampal network activity could rapidly and flexibly adjust to behavioral demands.

Voltage-dependent synaptic amplification likely facilitates dynamic changes in place-dependent activity that constitute a hallmark complexity of the hippocampal neural code. In addition, however, depolarization enhances the occurrence of dendritic plateau potentials and hence the synaptic plasticity likely underlying the formation of stable place-cell firing. Thus, modulation of membrane potential, through engagement of multiple mechanisms, likely affects not only the rapidly dynamic readout of the cognitive map, but also its more gradual formation and adaptation during learning.

STAR Methods

CONTACT FOR REAGENT AND RESOURCE SHARING

Further information and requests for resources and reagents should be directed to and will be fulfilled by the Lead Contact, Nelson Spruston (sprustonn@janelia.hhmi.org).

EXPERIMENTAL MODEL AND SUBJECT DETAILS

Rats—All animal procedures were approved by the Animal Care and Use Committee at the HHMI Janelia Research Campus, and all experiments conformed to relevant regulatory standards. Male, wildtype Wistar rats (RRID: RGD_13508588) used for *in-vitro* experiments were 3- to 8-weeks-old.

Mice—All animal procedures were approved by the Animal Care and Use Committee at the HHMI Janelia Research Campus, and all experiments conformed to relevant regulatory standards. Male, wildtype C57BL/6 mice used for *in-vivo* experiments were 10- to 17-weeks-old. Body weight check and quantitative health assessment were performed throughout the course of experiments according to protocols established at the HHMI Janelia Research Campus. Food was always provided *ad libitum*. After recovering from the surgery for head-plate affixation (see below), mice were placed on a water-restriction schedule (1.5 ml of water per day). On the third day after the surgery, a saucer training wheel was placed in the home cage.

METHOD DETAILS

Whole-cell patch-clamp recording in acute brain slices—3- to 8-week-old male Wistar rats were decapitated under deep isoflurane anesthesia, and the brain was transferred to an ice-cold dissection solution containing (in mM): 204.5 sucrose, 2.5 KCl, 1.25 NaH_2PO_4, 28 $NaHCO_3$, 7 dextrose, 3 Na-pyruvate, 1 Na-ascorbate, 0.5 $CaCl_2$, 7 $MgCl_2$ (pH 7.4, oxygenated with 95% CO_2 and 5% O_2). 250- or 350-μm-thick slices were sectioned at oblique angles using a vibrating tissue slicer (Leica VT 1200S, Leica Microsystems, Wetzlar, Germany). The CA3 and superficial layers of the entorhinal cortex were removed to limit polysynaptic activation by stimulating electrodes. The slices were then transferred to a suspended mesh within an incubation chamber filled with artificial cerebrospinal fluid (ACSF) containing (in mM): 125 NaCl, 2.5 KCl, 1.25 NaH_2PO_4, 25 $NaHCO_3$, 25 dextrose, 1.3 $CaCl_2$, 1 $MgCl_2$ (pH 7.4, oxygenated with 95% CO_2 and 5% O_2); 3 Na-pyruvate, 1 Na-ascorbate were added when dendritic recordings were performed. To test the sensitivity of the steeply voltage-dependent amplification to extracellular calcium level, another commonly used concentration (2 mM) was used for some experiments in Figure 1A and B; no statistical difference was found, so data were pooled together. After 30–60 minutes of recovery at 35–37°C, the chamber was maintained at room temperature.

All recordings were performed on slices submerged in the recording chamber of an upright microscope (BX61WI; Olympus, Tokyo, Japan) equipped with IR-DIC (infrared-differential interference contrast) microscopy and a water-immersion objective lens (40X, 0.80 NA or 60X, 1.00 NA; Olympus), constantly perfused with oxygenated ACSF at 33–35°C. SR-95531 (2 μM) and CGP 52432 (1 μM) were added to block $GABA_A$ and $GABA_B$ receptors, respectively (except for experiments in Figure 3B–D, S1A, S3I, J). Patch pipettes were pulled from thick-wall borosilicate glass, resulting in electric resistance of 3–9 MΩ when filled with an intracellular solution containing (in mM): 130 K-gluconate, 10 KCl, 10 Na_2-phosphocreatin, 10 HEPES, 4 Mg-ATP, 0.3 Na-GTP, and 0.2% biocytin (pH 7.2, osmolarity 295; 50 μM AF-594 was added when dendritic recordings were performed). In some early experiments with GABAergic inhibition blocked, 4 KCl and 135 K-gluconate were used instead, but no difference was found for these experiments. Reported membrane potentials were uncorrected for liquid junction potential.

Dendritic recordings were obtained on distal apical dendritic trunk 198–356 μm away from the soma. Patch-pipette series resistance was lower than 35 MΩ and 50 MΩ (with typical values of 20–30 MΩ) for somatic and dendritic recordings, respectively. At the end of the experiments, high-resolution Z-stack images were collected (using two-photon laser scanning microscopy as described previously, Kim et al., 2015) and used to determine the path distance of the recording site from the soma.

Current-clamp experiments in brain slices were performed with whole-cell patch-clamp recordings using a Dagan BVC-700A amplifier (Dagan Corporation, Minneapolis, MN). Data were low-pass-filtered with a cut-off frequency of 5 kHz and digitized at 50 kHz via BNC-2090 and BNC-2110 boards (National Instruments, Austin, TX) under the control of Prairie View and TriggerSync software (Prairie Technologies, Middleton, WI).

For activation of synapses, theta-glass micropipettes (~40–50 μm in diameter) filled with ACSF were used for bipolar stimulation via stimulus isolators (Model 4-AD, Getting Instruments, San Diego, CA). Stimulating electrodes were placed in the stratum lacunosum-moleculare (SLM) and the stratum radiatum (SR) ~200–300 μm away (toward subiculum) from the recorded cell to stimulate the perforant path (also known as temporoammonic path) and the Schaffer collaterals, thus recruiting synaptic inputs from the EC and the CA3 region, respectively. When the effects of both pathways were tested on the same neuron, stimulation of either one and both pathways was interleaved. In the experiments with GABAergic inhibition intact (Figure S1A), to facilitate recruitment of feedforward synaptic inhibition and minimize direct stimulation of inhibitory interneurons, the stimulating electrode was placed at least 650 μm away from the recorded cell. EPSPs were monitored every 20 seconds (10 seconds for some experiments in Figure S3I,J), and interleaved test pulses were used to monitor the recording quality (bridge balance and pipette capacitance compensation) and the input resistance of the cell throughout the experiment. To produce ramp-like EPSPs, stimulus patterns were modeled with the instantaneous input frequency modulated by a linear, symmetric ramp; for the trace examples and the summarized data reported, the stimulus used was generated with a peak frequency (at the center of the ramp) of ~50 Hz and a total duration of 1.2 seconds, but other parameters were also tested (see Results). To test the effects of theta rhythm on the synaptic amplification, theta-burst stimulation (TBS) was used, which consisted of five high-frequency bursts (5 stimuli at 100 Hz) repeated at an inter-burst interval of 200 ms (5 Hz). To generate simulated EPSPs using small synaptic current-like commands via the patch electrode, a custom-made voltage divider was applied to optimize the use of the full dynamic range of the digital-analog converter, thus producing simulated EPSPs that faithfully recaptured the smooth rise and decay kinetics of evoked responses.

Voltage-clamp experiments in brain slices were performed with whole-cell patch-clamp recordings using an Axopatch 200B amplifier (Axon Instruments, Molecular Devices, San Jose, CA), headstage cooling, and a low-pass Bessel filter applied at 5 kHz. Data sampling and digitization were done as described above. Patch pipettes with relatively low electric resistance (3–5 MΩ, when filled with the same intracellular solution as above) were used. To isolate persistent sodium current, a slow ramp command at a velocity of 10 mV/s (Carter et al., 2012) was used. The protocol was applied in the control condition first, followed by application of 1 μM TTX via the bath, and sodium current was defined by the result of subtracting the recording in TTX from the recording in control (TTX subtraction). We found that the voltage dependence of the persistent sodium current isolated in hippocampal slices was very similar to that observed using voltage clamp in acutely dissociated CA1 neurons (Carter et al., 2012), suggesting that the clamp quality is sufficient for a reasonable characterization of the perisomatic persistent sodium current in CA1 pyramidal neurons (see also Yamada-Hanff and Bean, 2013; Yamada-Hanff and Bean, 2015). In these experiments (Figure 3B–D), we used a voltage command consisting of a pre-pulse of 0 mV for 20 ms and then a jump to −20 mV for 10 ms, followed by a slow downward ramp from −20 mV to −80 mV at 10 mV/s. The brief pre-pulse and the reverse direction of the ramp were aimed to effectively push Na_V channels toward the equilibrium state between activation and inactivation (including slow inactivation, Park et al., 2013), thus reducing escape spiking; in contrast, blocking K_V and HCN channels did not prevent escape spiking (n=3 neurons from 3 rats). For one cell with the normal intracellular solution in which an upward ramp (same ramp speed) was applied, the result was similar without escape spiking, so the data were included. With intracellular low (0.5 mM) QX-314 (Figure 3C,D), although the persistent sodium current was nearly completely blocked, the rapid and transient sodium current in response to the voltage step of 0 mV clearly remained (normal intracellular solution, 11.0±2.5 nA, n=4 neurons from 2 rats; intracellular low QX-314, 11.5±4.5 nA, n=3 neurons from 2 rats; see also Hammarström and Gage, 1998). However, these values should be interpreted with caution, because of the likelihood of imperfect voltage-clamp of the axons (which contain a high density of $\mathrm{Na_V}$ channels). Ramp-induced current was monitored with an interval of at least 10–30 seconds, and interleaved test pulses were used to monitor the recording quality (series resistance compensation, whole-cell capacitive current cancellation, pipette capacitance compensation) and the input resistance of the cell throughout the experiment. Series resistance was 7–22 MΩ, and compensated up to 65% by the PREDICTION circuit (i.e., supercharging) and 60% by the CORRECTION circuit of the amplifier.

To assess the contribution of $\mathrm{K_V}$ and HCN channels to the synaptic amplification, we used $\mathrm{Ba^{2+}}$ and ZD7288. Given that blocking these channels alters dendritic cable properties (Golding et al., 2005; Hoffman et al., 1997) and possibly the effects of somatic steady current injection on the dendrites, the experiments were performed using somatically simulated synaptic responses. When $\mathrm{Ba^{2+}}$ or ZD7288 was applied (Figure S3I,J), amplification was assessed starting 10 minutes after the beginning of drug application; in the experiments using ZD7288, however, it was applied for only 5 minutes, followed by washout of the drug (i.e., washing in control ACSF again) for another 5 minutes to minimize time-dependent off-target effects (Harnett et al., 2015), and the lasting effects of the drug on HCN channels were evident in terms of hyperpolarized resting V_m, the block of voltage 'sag' (in response to hyperpolarizing test pulses) and the change of input resistance. Because blocking $\mathrm{K_V}$ or HCN channels results in reduction of net outward current upon depolarization, 1 μM TTX was subsequently applied via the bath to confirm that voltage-dependent amplification observed during the block is still driven by $\mathrm{Na_V}$ channels, rather than due to activation of additional voltage-dependent conductances. For the same reason that these blockers result in reduction of net outward current upon depolarization, cells in the presence of $\mathrm{Ba^{2+}}$ or ZD7288 were prone to regenerative activity resulting in part from subthreshold ionic currents (such as persistent sodium current; Yamada-Hanff and Bean, 2013) that led to continuous firing; we therefore used moderately low concentrations of $\mathrm{Ba^{2+}}$ (150 M) and ZD7288 (5 or 10 M), which were estimated to block approximately 35% of the A-type $\mathrm{K_V}$-channel conductance (Gasparini et al., 2007) and 40–50% of the HCN-channel conductance (Gasparini and DiFrancesco, 1997) in CA1 pyramidal neurons, respectively. Even at these concentrations, however, in some cases it was impossible to depolarize the cell (by steady current injection) to the same level as in the control condition (around −55 mV) without inducing excessive spiking; therefore, amplification was assessed at slightly less depolarized V_m (around −58 to −62 mV), and amplification in the subsequent TTX condition was measured at similar values of V_m for these cases. In two additional cells (from two rats) for which 10 μM ZD7288 was used, amplification could be assessed without runaway firing, and the results were found to be similar.

For all experiments using intracellular low QX-314, once the whole-cell configuration was established, we promoted activity-dependent block of $\mathrm{Na_V}$ channels by applying a series of step current injections to drive action potential firing; the effects stabilized within 2–3 minutes after break-in. To block NMDAR channels, the D-isomer of AP5 was used to maximize the effects. 20 nM (low) and 1 μM TTX were estimated to block ~50% and 100% of the $\mathrm{Na_V}$-channel conductance in hippocampal pyramidal neurons, respectively (Kim et al., 2015). For pharmacological experiments, the drugs were applied for at least 5–10 minutes before subsequent experiments commenced. Reagents were obtained from the following vendors. Sigma-Aldrich (St. Louis, MO): nickel chloride (Ni^{2+}), SR-95531, phenytoin, biocytin, sodium pyruvate, (+)-sodium L-ascorbate, phosphocreatine disodium, adenosine 5′-triphosphate magnesium (Mg-ATP), guanosine 5′-triphosphate sodium (Na-GTP), 4-(2-hydroxyethyl) piperazine-1-ethanesulfonic acid (HEPES), potassium D-gluconate, dextrose, barium chloride (Ba^{2+}). Fluka (St. Louis, MO): calcium chloride, magnesium chloride. Tocris Bioscience (Minneapolis, MN): D-(−)-2-amino-5-phosphonopentanoic acid (AP5), tetrodotoxin citrate (TTX), *N*-(2,6-Dimethylphenylcarbamoylmethyl)triethylammonium chloride (QX-314), nimodipine, CGP 52432, 2,3-dioxo-6-nitro-1,2,3,4-tetrahydrobenzo[*f*]quinoxaline-7-sulfonamide disodium salt (NBQX), 4-Ethylphenylamino-1,2-dimethyl-6-methylaminopyrimidinium chloride (ZD7288). Fisher Scientific (Fair Lawn, NJ): sodium chloride, potassium chloride, sodium bicarbonate, sodium phosphate monobasic, sucrose. Invitrogen (Waltham, MA): Alexa Fluor 594 hydrazide (AF-594). No blind design was used for experiments.

Surgery for in-vivo experiments—10- to 17-week-old male C57BL/6 mice were used for *in-vivo* patch-clamp recordings. Prior to behavioral training, a custom-made titanium head plate was affixed to the skull (first covered by cyanoacrylate glue) using dental acrylic under isoflurane anesthesia. To minimize the number of animals used, the head plates were designed to allow bilateral access of the hippocampus. Locations of craniotomy for electrophysiological recordings were marked (bregma: 1.6–1.7 mm AP, 1.9–2.0 mm ML for whole-cell recording, and 1.5–1.6 mm more posterior for field recording). Buprenorphine (0.0021 mg per 20 g body weight) was provided at the end of the surgery, and ketoprofen (0.01 mg per 20 g body weight) was used once per day in the next two days as a postoperative procedure.

Before the first electrophysiological recording on a given hemisphere, craniotomies of < 300 μm in diameter were performed under isoflurane anesthesia, and the dura was carefully preserved to enhance mechanical stability for underlying brain tissues. Silicon elastomer (Kwik-Cast; World Precision Instruments, Sarasota, FL) was used to seal the exposed skull and brain surface during recovery and between recording sessions.

Behavioral training in virtual reality—The behavioral setup based on a virtual-reality system was similar to Cohen et al. (2017). The animal was head-fixed on stainless-steel holders atop a hollow, lightweight polystyrene spherical treadmill (‘ball’) of 40 cm in diameter, with an infrared-based rotation tracking mechanism (Cohen et al., 2017; Sofroniew et al., 2014). The ball was surrounded by three thin-bezel monitors (463UN, NEC; frame rate, 60 Hz). This created a field of view encompassing 216° horizontally and 91° vertically (27° below and 64° above) from the eyes of the animal. The virtual environment rendering system using MouseoVeR (https://github.com/JaneliaSciComp/CohenBolstadLee_eLife2017) and Blender (www.blender.org) was developed as part of Janelia’s open-source virtual reality software platform (Jovian), and the animal’s location was sampled at 60 Hz (additional sampling occurred upon special events, such as detection of licking and reward delivery). The simulated environments were oval tracks of 150 cm × 12 cm, consisting of straight arms connected by turns, with a white ‘sky’ and salient visual features (black-and-white stripes and dots against high-contrast backgrounds) distributed on the walls and the floor, which were designed to have the size and contrast for optimal stimuli, based on our knowledge about the sensory tuning properties of visual cortical neurons in mice (e.g., Zhao et al., 2013). Animals were trained to run unidirectionally in order to receive rewards of 10% sucrose solution through a lick port delivered at two fixed locations.

On the third day following the surgery of head-plate implantation, a saucer training wheel was placed in the home cage. After recovering for a total of about one week, mice were placed on a water-restriction schedule (1.5 ml of water per day). Behavioral training started following one week of water restriction. After initial acclimatization to the rig on one short session, mice received training for a total of 10 days, with 2–3 sessions of ~15–20 minutes each on the first 2–3 days, followed by single-session training with the duration gradually increased to a total of 60–70 minutes. Each day, after training was completed, additional water was supplemented to ensure a total water consumption of 1.5 ml. In typical recording sessions following all training, mice ran continuously without signs of distress and discomfort, and swung their bodies at turns smoothly even with minimal automated heading involved (see also Cohen et al., 2017). They also exhibited licking in anticipation of the arrival at reward delivery sites, which suggests learning of the spatial contingency for the task.

Whole-cell patch-clamp recording in awake mice during virtual navigation— After half a day to a full day of recovery from the surgery of craniotomy, recordings were performed for 2–3 consecutive days from each hemisphere. To map the depth of the somatic layer of pyramidal neurons (stratum pyramidale) in the dorsal hippocampal CA1 region, a long-taper extracellular recording pipette with electric resistance of < 3 MΩ (when filled with 0.9% NaCl) was inserted vertically to the rostral craniotomy in order to detect theta-modulated unit activity and sharp waves, which was typically 1.1–1.3 mm below the surface of the brain. After the depth was determined, a glass pipette for recording local field potential was inserted into the caudal craniotomy at an angle of 45° and advanced until near the CA1 stratum pyramidale, as determined by trigonometry. The pipette for mapping recording depths was discarded, and a long-taper patch pipette with electric resistance of 8–13 MΩ (when filled with the same intracellular solution as used for *in-vitro* electrophysiology) was inserted vertically into the rostral craniotomy, advancing through the neocortex with a positive pressure of 8–9 psi, which was then reduced to ~0.4 psi upon entry into the hippocampus. Somatic whole-cell recordings were obtained using the “blind-patch” technique (Blanton et al., 1989). All recordings accepted for analyses had the canonical electrophysiological signatures of CA1 pyramidal neurons (Harvey et al., 2009; Lee et al., 2012). After breaking in to achieve the whole-cell configuration, the characteristic activity of CA1 pyramidal neurons, including prominent fluctuations of subthreshold V_m and theta oscillations, were typically preceded by a short period (usually less than a minute, but in some cases up to ~3 minutes) of significantly low activity with hyperpolarized V_m; no data were used for analyses until V_m settled at values typically in the range of −70 to −50 mV. Bridge balance was carefully monitored and adjusted throughout the experiment. Patch-pipette series resistance was typically around 20–80 MΩ. In the 7 neurons patched with normal intracellular solution, 2 of them had spatially modulated ramp-like synaptic responses (see below) that drove action potential firing in the absence of somatic current injection, and the others were silent cells. In 4 of these silent cells, spatially modulated firing fields were induced using a large, short current pulse injected to the soma (Bittner et al., 2015) for another experimental purpose, and the voltage dependence of synaptic responses was assessed in this condition; no statistical difference was found between voltage-dependent amplification in neurons with native and induced spatially dependent activity. For experiments in which low QX-314 was applied intracellularly, a series of step pulses were applied to evoke action potentials once whole-cell configuration was established, until the reduction of firing rate stabilized, which occurred within 3 minutes (at 2–3 minutes after break-in, firing rate was 56±3% compared to 1 minute after break-in). In the 6 neurons patched with intracellular low QX-314, 4 of them had spatially modulated ramp-like synaptic responses that drove action potential firing in the absence of somatic current injection. We chose a lower concentration of QX-314 than typically used in other studies, in order to minimize potential problems associated with the known off-target effects (Kim et al., 2015). Furthermore, prior experience indicated that higher concentrations (~5 mM) of QX-314 included in the patch electrode used with *in-vivo* blind-patch procedure resulted in obvious reduction of spontaneous V_m fluctuations (in the visual cortex), suggesting unexpected effects on circuit excitability (X.Z., unpublished data). The following observations suggest that low QX-314 included in the patch electrode does not produce network-wide effects that influence the synaptic inputs received by the recorded cells: First, 5/6 neurons (from 6 mice) recorded with intracellular low QX-314 still exhibited position-dependent modulation of V_m in the absence of current injection (Figure 7B), which in some cells drove clear spatially dependent firing. Second, the estimates of power spectral density (PSD) that characterizes subthreshold V_m, which is predominantly influenced by ongoing synaptic activity from the network, were very similar in the normal and the intracellular low-QX-314 conditions, especially for the theta (4–10 Hz) band (Figure S7C), the frequency range particularly characteristic of high-frequency synaptic inputs received by the dendrites of CA1 pyramidal neurons (Vaidya and Johnston, 2013). Third, the sizes of spatially dependent ramp-like responses at the comparable and relatively hyperpolarized V_m were not different between the neurons patched with the normal intracellular solution or intracellular low QX-314 ($p > 0.05$ by Student’s t-test for comparison using either the standard deviation of average spatial profiles or the amplitude of spatially modulated synaptic ramps; Figure 7C).

Current-clamp experiments *in vivo* were performed with whole-cell patch-clamp recordings using a Dagan BVC-700A amplifier (Dagan Corporation). Data were low-pass-filtered with a cut-off frequency of 5 kHz and digitized at 20 kHz via an ITC18 digital-analog converter (HEKA Instrutech, Bellmore, NY) under the control of WaveSurfer software (wavesurfer.janelia.org). No blind design was used for experiments.

Computational modeling—Numerical simulations were performed using two computational models with different levels of details, constrained by data (see below) that were collected independently of our experimental design and observations made in this study. Therefore, we view the results of the simulations as *predictions* from these models, as opposed to recreation of observed phenomena by tuning model parameters in order to match experimental data. These simulations serve as independent tests for the conceptual mechanistic model we formed in this paper.

All simulations were performed using the NEURON simulation environment (Hines and Carnevale, 1997), interfaced with Python (Hines et al., 2009) as needed, with a fixed time step (for the simple model, *dt*=0.025 ms; for the full model, *dt*=0.02 ms). Results were analyzed using custom software programmed in *hoc* or extending the open-source tools in Python (Jones et al., 2001).

For the simple model, we constructed a single-compartmental model with the input resistance and the membrane time constant consistent with the recordings of rat CA1 pyramidal neurons, using specific membrane capacitance (C_m) of 1 μF/cm^2, axial resistivity (R_i) of 35.4 Ω·cm and a leak conductance of 60 μS/cm^2 with the reversal potential of −70 mV. This model also contained an active conductance simulating conventional Na_v channels that mediate firing of axonal action potentials, using a Markovian kinetic scheme (Carter et al., 2012) with a Q_{10} of 2.3 included (adapted as an *NMODL* format by Nathan Gouwens; Gouwens et al., 2018); the voltage dependence of the channel model was adjusted to revert the correction of liquid junction potential used in Carter et al. (2012). The Na_v-channel density was constrained by the measurement of the sustained, TTX-sensitive sodium current recorded at the soma of acutely dissociated CA1 pyramidal neurons (Carter et al., 2012) using a simulated voltage-clamp process, which provided a value of 2.75 mS/cm^2 and resulted in a physiologically realistic apparent voltage threshold for spike initiation of −52 mV (in response to the smallest simulated EPSP that triggered a spike, at the resting V_m of the model; Royeck et al., 2008) and a resting membrane potential of −69.8 mV. Synaptic activation was simulated as a high-frequency burst of 5 presynaptic stimuli at 100 Hz, with the synaptic conductance modeled as a difference of two exponentially decaying functions, using a peak conductance of 0.05 nS (Figure 5A) and rise and decay time constants of 2 and 20 ms to recapture the amplitude and the kinetics of burst EPSPs (at or near the resting V_m) observed in our somatic recordings. Synaptic current was modeled as a current source to compensate for unrealistic reduction in driving force upon depolarization in the single-compartment model. We also tested synaptic amplification using conductances simulating conventional Na_v channels with Hodgkin-Huxley mechanisms instead (Branco et al., 2016; Kim et al., 2015; see Results). For simulating voltage-clamp experiments, the single EPSP waveform (Figure 5B, *right*) was constructed with the kinetics comparable to our experimental recordings and the peak amplitude closely matching the burst EPSP waveform used (Figure 5B, *left*). The temperature tested in the simulations was 33–37°C; data reported in the figures were simulated using 33°C.

For the full model, we employed a morphologically and biophysically detailed multi-compartmental model of a mouse CA1 pyramidal neuron (Grienberger et al., 2017), without any further tuning of the model parameters. This model reproduces many aspects of place-cell responses and recapitulates the biophysical properties of dendritic integration described in a wealth of experimental literature (see Grienberger et al., 2017 for details). Axon hillock, axon initial segment (AIS), axon and dendritic spines were explicitly modeled, constrained by high-resolution anatomical data derived from reconstructions using array tomography

(Bloss et al., 2016). The model included a leak conductance and active conductances which simulated the following ion channels using Hodgkin-Huxley-style mechanisms, with different channel densities and spatial gradients: Na_v channels, A-type, M-type and delayed-rectifier K_v channels, and HCN channels. Note that the voltage dependence and the density of Na_v channels at the soma and at the AIS were tuned using the properties of action potentials in CA1 pyramidal neurons (the half-activation voltage for the transient current at the AIS ~3 mV more hyperpolarized than at the soma, Royeck et al., 2008) as the only optimization target, resulting in action potentials initiated first at the AIS with an apparent voltage threshold measured at the soma −52 mV. Synaptic activation was simulated as a high-frequency burst of 5 presynaptic stimuli at 100 Hz, with the α-amino-3-hydroxy-5-methyl-4-isoxazolepropionic-acid (AMPA)- and the *N*-methyl-D-aspartate (NMDA)-type glutamate receptor conductance modeled using Markovian kinetic schemes. Activated synapses were randomly chosen from the apical dendritic arbor. To yield burst EPSPs with peak amplitudes at the resting V_m of the model comparable across the control and simulated drug conditions (low TTX and AP5) and between sites of current injection, for the simulations with somatic V_m modulation (Figure 5C, S4B, C), 5 synapses were used in control and simulated low TTX, and 7 synapses were used in simulated 50 μM AP5; for the simulations with dendritic V_m modulation (Figure S4B), 3 synapses were used. For the modulation of dendritic V_m, the range of V_m tested was the same as for the modulation of somatic V_m. For the simulations involving block of A-type K_v channels or HCN channels (Figure S5), synaptic responses were simulated using EPSC-like current waveforms injected to the soma to parallel the experiments (Figure S3I, J; see Results), and the current was adjusted to yield burst EPSPs with peak amplitudes at the resting V_m of the model comparable across the control and simulated drug conditions. To simulate bath application of 20 nM TTX (Figure 5C, S4C) and 1 μM TTX (Figure S5), the conductance of Na_v channels in all compartments was reduced to 50% of control and zero, respectively; to simulate bath application of 50 μM AP5, the conductance of NMDAR channels at all synapses was reduced to zero; to simulate bath application of 5 μM ZD7288, the conductance of HCN channels in all compartments was reduced to 60% of control; to simulate bath application of 150 μM Ba^{2+}, the conductance of A-type K_v channels in all compartments was reduced to 65% of control. The temperature used in the simulations was 35°C.

QUANTIFICATION AND STATISTICAL ANALYSIS

To estimate synaptic inputs received by the neurons recorded *in vitro*, peak amplitude and integral of synaptic responses were measured from recordings with somatic action potentials and associated spike-dependent effects removed. We used the following spike removal procedure, with effects similar to Lee et al. (2012) and Epsztein et al. (2011): all data points associated with the period between 3 ms before and 20 ms after the peak of an action potential were removed, then replaced by data generated based on linear interpolation; however, if the end of the period had fallen within the spike-removal period of another action potential, the definition of this period extended to include until 20 ms after the next action potential. Empirically, this was sufficient to remove data points containing effects attributable to somatic action potential firing (such as afterdepolarizations and afterhyperpolarizations) in *in-vitro* conditions (Anwyl, 1999; Bean, 2007; Magee and

Carruth, 1999; Park et al., 2010; Su et al., 2001). Although this simple approach was less effective for removing plateau potentials (presumably of dendritic origin; Takahashi and Magee, 2009), spike removal was not required for the *in-vitro* experiments where plateau potentials were observed (Figure 8, S8). Furthermore, in the cases for burst EPSPs, the spike removal always resulted in a peak depolarization just prior to the initiation of the first action potential in trials with somatic firing, therefore eliminating any contribution of spike-driven activity to our measurement of response peak amplitude. In the cases for ramp-like EPSPs, the effectiveness of this procedure for removing effects of spike-dependent ionic currents was difficult to assess. Nevertheless, in every neuron tested, we observed prominent voltage-dependent amplification of synaptic responses either prior to the first spike in trials with action potential firing or in trials without firing at all, regardless of the stimulus pattern used as long as the resultant EPSPs manifested significant temporal summation (Figure 1B,C, and see Results). These observations and considerations argue against the possibility that the synaptic amplification is a pure spike-dependent phenomenon.

To determine the baseline V_m where the steepest transition for the relationship between synaptic response measure vs. baseline V_m (Figure 1) occurred (referred to as “transition V_m” in the text; analogous to $V_{m,gate}$ in Lee et al., 2012) for each neuron in a manner comparable to Lee et al. (2012), we used a similar procedure, described as follows. For a given cell, it was defined as the average baseline V_m (selected from one of the pairs of trials with nearest-neighbored baseline V_m’s in the recording) that maximized the difference between the means of the measure for all responses above and below the selected V_m. To align relationships between synaptic response measure vs. baseline V_m from multiple neurons (Figure 1), for each cell, values of the response measure were normalized by the average measure of the responses at around −75 to −65 mV, and the transition V_m was subtracted from associated baseline V_m values. Amplification ratio was calculated as the ratio of the average measure of responses at around −55 to −50 mV (the most depolarized baseline V_m possibly tested without continuous, pacemaker-like firing activity) to the average measure of responses at around −70 to −65 mV. For each level of baseline V_m, 5–20 trials were obtained for the somatic recordings and 2–4 trials were obtained for the dendritic recordings performed in brain slices; although fewer trials per V_m were obtained for the dendritic recordings, more baseline V_m levels were tested so that the dendritic recordings had the total number of trials per cell comparable to the somatic recordings, yet with an improved resolution in terms of baseline V_m value. To assess the sensitivity of subthreshold responses to low TTX (Figure S8A,B), for some cells in control in which a small nonlinear component was observed in the late phase of burst EPSPs in response to relatively strong synaptic stimulation (putative regenerative dendritic events evident as a discontinuity of dV/dt; Kim et al. 2015), peak amplitude was measured at a time prior to the small nonlinear component, and responses in low TTX were measured at the same time point as in control. Dendritic plateau probability was calculated as the number of trials with dendritic plateau potential observed normalized by the number of total trials; experiments with a total of 9 stimulus intensities applied in 7 cells were used (Figure 8C).

In the voltage-clamp experiments (Figure 3B–D), recordings were corrected for leak and capacitive currents by the TTX subtraction procedure (see above), and the current level immediately following the ramp-induced current was taken as baseline. Subthreshold persistent sodium current was quantified (Figure 3D) by averaging current measurements between 49.9 and 50.1 mV of the current-voltage (I-V) relationship, and 8–27 trials (typically 15–25 trials) were used for each condition (control or TTX).

In order to plot V_m as a function of the animal's position during virtual movement in a simulated environment *in vivo* (Figure 7, S7), the data were processed as below. The position was a linearized representation of the animal's location by collapsing a virtual environment and mapping the spatial locations to the midline along the oval-shaped track. Because the sampling of animal's location was performed at a lower rate than the electrophysiological signals, a linearly interpolated position was assigned for each sample of V_m at the corresponding time. To reveal the slow envelope of V_m as a representation of temporally summated responses to synaptic inputs received by the neuron, fast action potentials were removed by temporal filtering using a median filter with a window of 10 ms, and fast subthreshold fluctuations were removed by further temporal filtering using a low-pass filter with a cut-off frequency of 2 Hz. A cut-off for movement speed of 3 cm/s was set to exclude data recorded during slow motion from all of the analyses. Finally, the filtered V_m recorded during running was plotted as a function of the animal's linearized position and linearly resampled using a spatial bin of 0.1 cm. To confirm that these procedures did not distort the characterization of prolonged, ramp-like spatially dependent synaptic responses, effects of the filtering and the bin size used were checked, by comparing between the spatial profiles of raw V_m, spike-removed V_m and further low-pass-filtered V_m, made with a spatial bin of 0.1 cm (by linear resampling) or 4 cm (by spatial averaging; Cohen et al. 2017; Lee et al., 2012). Baseline V_m for each lap was determined as the mean of the V_m values associated with the spatial bins with the most hyperpolarized 10% V_m's. To determine whether the responses of a cell is spatially modulated, for the spatial profiles of baseline-subtracted, low-pass-filtered V_m from individual laps and their average, candidate place fields were first defined by all contiguous spatial bins around the maximum V_m with the associated V_m ¥ 30% of the maximum V_m, and spatial modulation was claimed when the candidate field from the average spatial profile was larger than 12 cm and overlapped with candidate fields from more than 2/3 of the individual laps. The amplification ratio of synaptic responses recorded *in vivo* was calculated in two ways (Figure 7C). Given the strong spatial coherence between responses at different baseline V_m (Figure S7A), to measure amplification based on the variance of activity, the standard deviation of an entire average spatial profile of low-pass-filtered V_m was used. To measure amplification based on the amplitude and the integral of place-dependent responses, an average spatial profile of baseline-subtracted, low-pass-filtered V_m was first fitted with a von Mises function (circular normal distribution) which allowed up to two skewed bell-shaped peaks in the following form:

$$y = \sum_{i=1,2} A_i * e^{(k_i * (\cos((x - peak_i) + skewness_i * (\cos(x - peak_i) - 1)) - 1))}$$

Spatially modulated synaptic ramps were identified as peaks with an amplitude larger than two times standard deviation of the spatial profile; peak amplitude was calculated as the mean of V_m within a window of 5 cm centered on the peak position of the ramp with a larger amplitude, and integral was calculated from the entire spatial profile. Finally, amplification ratio was taken as the ratio of the measure from depolarized laps to the measure from reference laps. We assessed amplification in two different ways because the measurements using peak amplitude and integral are formalisms consistent with the method used for *in-vitro* data, but quantification using the standard deviation of spatial profiles can be performed without a relatively arbitrary definition of baseline V_m for *in-vivo* conditions; furthermore, it considers amplification based on entire activity profiles rather than particular place fields. Caution should be taken in considering direct comparison between the absolute amplifications assessed *in vitro* and *in vivo* that were based on peak amplitude and integral. Only recordings from complete laps and without application of any test pulses were used for analyses. For each level of baseline V_m, recordings from 3–13 laps (12±1 laps per neuron) were used for quantification, with the only exception of a cell patched with intracellular low QX-314; in this case, recording from 2 laps at the most depolarized baseline V_m was used as a conservative estimate for voltage-dependent amplification in the low-QX-314 condition, although using the data recorded from 6 laps at the next most depolarized V_m instead gave the same result. Power spectral density was estimated using Welch's method with a Hamming window, performed on ~10–50 seconds of initial recordings in the absence of current injection and somatic action potentials. For logarithmic representation of power spectrum (Figure S7C), PSD was expressed in decibels (dB), defined as $10 \cdot \log_{10}(\mathrm{PSD})$.

Compared with the approach used by Lee et al. (2012) and Epsztein et al. (2011), we used simpler procedures of spike removal for our *in-vivo* data. As a precaution, therefore, we used a second approach, relying on the analyses of relatively small, or initially quiescent, spatially dependent synaptic responses (see Results; Figure S7B,D) to show that the synaptic amplification observed *in vivo* is strongly supported by a mechanism independent of action potential firing.

Analyses were performed using IGOR Pro (Wavemetrics, Lake Oswego, OR), MATLAB (The MathWorks, Natick, MA), Microsoft Office Excel (Microsoft, Redmond, WA), and ImageJ (National Institutes of Health, Bethesda, MD).

Data were presented as mean±S.E.M. In one exception, a relative error estimate was used to present data as mean±4.34*S.E.M./mean for logarithmic representation of PSD (Figure S7C). In bar graphs, data from individual cells are presented as scatter plots or point clouds (in gray). Statistical analyses were performed using OriginPro (OriginLab Corporation, Northampton, MA) and IGOR Pro. Reported p values were all based on two-tailed tests.

DATA AND SOFTWARE AVAILABILITY

The software for the virtual-reality rendering system MouseoVeR can be obtained at: https://github.com/JaneliaSciComp/CohenBolstadLee_eLife2017. The software for data acquisition and device control WaveSurfer can be downloaded at: https://wavesurfer.janelia.org. All data presented in the figures are deposited to Figshare (Hsu et al., 2018; https://doi.org/10.25378/janelia.5468860). Code for simulations are publicly available on the ModelDB database and GitHub. The accession number for the computational models reported in this paper is ModelDB: 240960. Links to these resources are provided on our laboratory website (https://www.janelia.org/lab/spruston-lab/resources).

Supplementary Material

Refer to Web version on PubMed Central for supplementary material.

Acknowledgments

We thank A. Lee and J. Cohen for original design of the virtual-reality system; I. Soltesz for computational resources and discussion; A. Lee, D. Lee, B. Bean, J. Magee, J. Cohen, B. Carter, S. Romani, B. Mensh and the Spruston lab for scientific discussion; M. Harnett, S. Vaidya and M. Cembrowski for technical advice. This work was made possible by funding from the Howard Hughes Medical Institute and NIH BRAIN Initiative U19 award NS104590 (I. Soltesz, A.D.M.).

References

Ainge JA, van der Meer MA, Langston RF, Wood ER. Exploring the role of context-dependent hippocampal activity in spatial alternation behavior. Hippocampus. 2007; 17:988–1002. [PubMed: 17554771]

Anwyl R. Metabotropic glutamate receptors: electrophysiological properties and role in plasticity. Brain research Brain research reviews. 1999; 29:83–120. [PubMed: 9974152]

Bean BP. The action potential in mammalian central neurons. Nature reviews Neuroscience. 2007; 8:451–465. [PubMed: 17514198]

Bittner KC, Grienberger C, Vaidya SP, Milstein AD, Macklin JJ, Suh J, Tonegawa S, Magee JC. Conjunctive input processing drives feature selectivity in hippocampal CA1 neurons. Nature neuroscience. 2015; 18:1133–1142. [PubMed: 26167906]

Bittner KC, Milstein AD, Grienberger C, Romani S, Magee JC. Behavioral time scale synaptic plasticity underlies CA1 place fields. Science. 2017; 357:1033–1036. [PubMed: 28883072]

Blanton MG, Lo Turco JJ, Kriegstein AR. Whole cell recording from neurons in slices of reptilian and mammalian cerebral cortex. Journal of neuroscience methods. 1989; 30:203–210. [PubMed: 2607782]

Bloss EB, Cembrowski MS, Karsh B, Colonell J, Fetter RD, Spruston N. Structured dendritic inhibition supports branch-selective integration in CA1 pyramidal cells. Neuron. 2016; 89:1016–1030. [PubMed: 26898780]

Branco T, Tozer A, Magnus CJ, Sugino K, Tanaka S, Lee AK, Wood JN, Sternson SM. Near-Perfect Synaptic Integration by Nav1.7 in Hypothalamic Neurons Regulates Body Weight. Cell. 2016; 165:1749–1761. [PubMed: 27315482]

Carter BC, Giessel AJ, Sabatini BL, Bean BP. Transient sodium current at subthreshold voltages: activation by EPSP waveforms. Neuron. 2012; 75:1081–1093. [PubMed: 22998875]

Castro-Alamancos MA, Rigas P, Tawara-Hirata Y. Resonance (approximately 10 Hz) of excitatory networks in motor cortex: effects of voltage-dependent ion channel blockers. The Journal of physiology. 2007; 578:173–191. [PubMed: 16945964]

Chao TI, Alzheimer C. Effects of phenytoin on the persistent Na+ current of mammalian CNS neurones. Neuroreport. 1995; 6:1778–1780. [PubMed: 8541480]

Cobb S, Lawrence JJ. Neuromodulation of hippocampal cells and circuits In Hippocampal Microcircuits: A computational Modeler's Resource Book. Cutsuridis V, Graham BP, Cobb S, Vida I, editorsHeidelberg, Germany: Springer; 2010.

Cohen JD, Bolstad M, Lee AK. Experience-dependent shaping of hippocampal CA1 intracellular activity in novel and familiar environments. eLife. 2017; 6

Colbert CM, Pan E. Ion channel properties underlying axonal action potential initiation in pyramidal neurons. Nature neuroscience. 2002; 5:533–538. [PubMed: 11992119]

Colom LV, Castaneda MT, Reyna T, Hernandez S, Garrido-Sanabria E. Characterization of medial septal glutamatergic neurons and their projection to the hippocampus. Synapse. 2005; 58:151–164. [PubMed: 16108008]

Crill WE. Persistent sodium current in mammalian central neurons. Annual review of physiology. 1996; 58:349–362.

Danielson NB, Zaremba JD, Kaifosh P, Bowler J, Ladow M, Losonczy A. Sublayer-Specific Coding Dynamics during Spatial Navigation and Learning in Hippocampal Area CA1. Neuron. 2016; 91:652–665. [PubMed: 27397517]

Derdikman D, Knierim JJ. Space, Time and Memory in the Hippocampal Formation. Heidelberg Germany: Springer-Verlag Wien; 2014.

Domnisoru C, Kinkhabwala AA, Tank DW. Membrane potential dynamics of grid cells. Nature. 2013; 495:199–204. [PubMed: 23395984]

Eichenbaum H, Dudchenko P, Wood E, Shapiro M, Tanila H. The hippocampus, memory, and place cells: is it spatial memory or a memory space? Neuron. 1999; 23:209–226. [PubMed: 10399928]

Epsztein J, Brecht M, Lee AK. Intracellular determinants of hippocampal CA1 place and silent cell activity in a novel environment. Neuron. 2011; 70:109–120. [PubMed: 21482360]

Fenton AA, Lytton WW, Barry JM, Lenck-Santini PP, Zinyuk LE, Kubik S, Bures J, Poucet B, Muller RU, Olypher AV. Attention-like modulation of hippocampus place cell discharge. The Journal of neuroscience: the official journal of the Society for Neuroscience. 2010; 30:4613–4625. [PubMed: 20357112]

Frank LM, Brown EN, Wilson M. Trajectory encoding in the hippocampus and entorhinal cortex. Neuron. 2000; 27:169–178. [PubMed: 10939340]

Frank LM, Stanley GB, Brown EN. Hippocampal plasticity across multiple days of exposure to novel environments. The Journal of neuroscience: the official journal of the Society for Neuroscience. 2004; 24:7681–7689. [PubMed: 15342735]

French CR, Sah P, Buckett KJ, Gage PW. A voltage-dependent persistent sodium current in mammalian hippocampal neurons. J Gen Physiol. 1990; 95:1139–1157. [PubMed: 2374000]

Freund TF, Antal M. GABA-containing neurons in the septum control inhibitory interneurons in the hippocampus. Nature. 1988; 336:170–173. [PubMed: 3185735]

Fuhrmann F, Justus D, Sosulina L, Kaneko H, Beutel T, Friedrichs D, Schoch S, Schwarz MK, Fuhrmann M, Remy S. Locomotion, Theta Oscillations, and the Speed-Correlated Firing of Hippocampal Neurons Are Controlled by a Medial Septal Glutamatergic Circuit. Neuron. 2015; 86:1253–1264. [PubMed: 25982367]

Gasparini S, DiFrancesco D. Action of the hyperpolarization-activated current (Ih) blocker ZD 7288 in hippocampal CA1 neurons. Pflugers Archiv: European journal of physiology. 1997; 435:99–106. [PubMed: 9359908]

Gasparini S, Losonczy A, Chen X, Johnston D, Magee JC. Associative pairing enhances action potential back-propagation in radial oblique branches of CA1 pyramidal neurons. The Journal of physiology. 2007; 580:787–800. [PubMed: 17272353]

Gasparini S, Magee JC. Phosphorylation-dependent differences in the activation properties of distal and proximal dendritic Na+channels in rat CA1 hippocampal neurons. The Journal of physiology. 2002; 541:665–672. [PubMed: 12068031]

Golding NL, Mickus TJ, Katz Y, Kath WL, Spruston N. Factors mediating powerful voltage attenuation along CA1 pyramidal neuron dendrites. The Journal of physiology. 2005; 568:69–82. [PubMed: 16002454]

Golding NL, Spruston N. Dendritic sodium spikes are variable triggers of axonal action potentials in hippocampal CA1 pyramidal neurons. Neuron. 1998; 21:1189–1200. [PubMed: 9856473]

Gouwens NW, Berg J, Feng D, Sorensen SA, Zeng H, Hawrylycz MJ, Koch C, Arkhipov A. Systematic generation of biophysically detailed models for diverse cortical neuron types. Nat. Commun. 2018; 9:710. [PubMed: 29459718]

Grienberger C, Milstein AD, Bittner KC, Romani S, Magee JC. Inhibitory suppression of heterogeneously tuned excitation enhances spatial coding in CA1 place cells. Nature neuroscience. 2017; 20:417–426. [PubMed: 28114296]

Hammarstrom AK, Gage PW. Inhibition of oxidative metabolism increases persistent sodium current in rat CA1 hippocampal neurons. The Journal of physiology. 1998; 510(Pt 3):735–741. [PubMed: 9660889]

Harnett MT, Magee JC, Williams SR. Distribution and function of HCN channels in the apical dendritic tuft of neocortical pyramidal neurons. The Journal of neuroscience: the official journal of the Society for Neuroscience. 2015; 35:1024–1037. [PubMed: 25609619]

Harvey CD, Collman F, Dombeck DA, Tank DW. Intracellular dynamics of hippocampal place cells during virtual navigation. Nature. 2009; 461:941–946. [PubMed: 19829374]

Hasselmo ME, Giocomo LM. Cholinergic modulation of cortical function. Journal of molecular neuroscience: MN. 2006; 30:133–135. [PubMed: 17192659]

Hines ML, Carnevale NT. The NEURON simulation environment. Neural computation. 1997; 9:1179–1209. [PubMed: 9248061]

Hines ML, Davison AP, Muller E. NEURON and Python. Frontiers in neuroinformatics. 2009; 3:1. [PubMed: 19198661]

Hoffman DA, Magee JC, Colbert CM, Johnston D. K+ channel regulation of signal propagation in dendrites of hippocampal pyramidal neurons. Nature. 1997; 387:869–875. [PubMed: 9202119]

Hollup SA, Molden S, Donnett JG, Moser MB, Moser EI. Accumulation of hippocampal place fields at the goal location in an annular watermaze task. The Journal of neuroscience: the official journal of the Society for Neuroscience. 2001; 21:1635–1644. [PubMed: 11222654]

Hsu CL, Zhao X, Milstein AD, Spruston N. Persistent sodium current mediates the steep voltage dependence of spatial coding in hippocampal pyramidal neurons: Source data for all figures. Figshare. 2018. http://dx.doi.org/10.25378/janelia.5468860

Hu H, Vervaeke K, Storm JF. Two forms of electrical resonance at theta frequencies, generated by M-current, h-current and persistent Na+current in rat hippocampal pyramidal cells. The Journal of physiology. 2002; 545:783–805. [PubMed: 12482886]

Hu W, Tian C, Li T, Yang M, Hou H, Shu Y. Distinct contributions of Na(v)1.6 and Na(v)1.2 in action potential initiation and backpropagation. Nature neuroscience. 2009; 12:996–1002. [PubMed: 19633666]

Ito HT, Zhang SJ, Witter MP, Moser EI, Moser MB. A prefrontal-thalamo-hippocampal circuit for goal-directed spatial navigation. Nature. 2015; 522:50–55. [PubMed: 26017312]

Jones E, Oliphant E, Peterson P. , et al. SciPy: Open source scientific tools for Python. 2001. http://www.scipy.org

Kim Y, Hsu CL, Cembrowski MS, Mensh BD, Spruston N. Dendritic sodium spikes are required for long-term potentiation at distal synapses on hippocampal pyramidal neurons. eLife. 2015; 4

Kole MH, Ilschner SU, Kampa BM, Williams SR, Ruben PC, Stuart GJ. Action potential generation requires a high sodium channel density in the axon initial segment. Nature neuroscience. 2008; 11:178–186. [PubMed: 18204443]

Kuo CC, Bean BP. Slow binding of phenytoin to inactivated sodium channels in rat hippocampal neurons. Molecular pharmacology. 1994; 46:716–725. [PubMed: 7969051]

Larkum ME, Zhu JJ, Sakmann B. A new cellular mechanism for coupling inputs arriving at different cortical layers. Nature. 1999; 398:338–341. [PubMed: 10192334]

Lee D, Lin BJ, Lee AK. Hippocampal place fields emerge upon single-cell manipulation of excitability during behavior. Science. 2012; 337:849–853. [PubMed: 22904011]

Leranth C, Frotscher M. Cholinergic innervation of hippocampal GAD- and somatostatin-immunoreactive commissural neurons. The Journal of comparative neurology. 1987; 261:33–47. [PubMed: 2887594]

Leutgeb S, Leutgeb JK, Barnes CA, Moser EI, McNaughton BL, Moser MB. Independent codes for spatial and episodic memory in hippocampal neuronal ensembles. Science. 2005; 309:619–623. [PubMed: 16040709]

Lorincz A, Nusser Z. Molecular Identity of Dendritic Voltage-Gated Sodium Channels. Science. 2010; 328:906–909. [PubMed: 20466935]

Magee JC, Carruth M. Dendritic voltage-gated ion channels regulate the action potential firing mode of hippocampal CA1 pyramidal neurons. Journal of neurophysiology. 1999; 82:1895–1901. [PubMed: 10515978]

Magee JC, Johnston D. Characterization of single voltage-gated Na+ and Ca2+ channels in apical dendrites of rat CA1 pyramidal neurons. The Journal of physiology. 1995; 487:67–90. [PubMed: 7473260]

Major G, Larkum ME, Schiller J. Active properties of neocortical pyramidal neuron dendrites. Annual review of neuroscience. 2013; 36:1–24.

Markus EJ, Qin YL, Leonard B, Skaggs WE, McNaughton BL, Barnes CA. Interactions between location and task affect the spatial and directional firing of hippocampal neurons. The Journal of neuroscience: the official journal of the Society for Neuroscience. 1995; 15:7079–7094. [PubMed: 7472463]

Monaco JD, Rao G, Roth ED, Knierim JJ. Attentive scanning behavior drives one-trial potentiation of hippocampal place fields. Nature neuroscience. 2014; 17:725–731. [PubMed: 24686786]

Muller RU, Kubie JL. The effects of changes in the environment on the spatial firing of hippocampal complex-spike cells. The Journal of neuroscience: the official journal of the Society for Neuroscience. 1987; 7:1951–1968. [PubMed: 3612226]

O'Keefe JA. Place units in the hippocampus of the freely moving rat. Experimental neurology. 1976; 51:78–109. [PubMed: 1261644]

O'Keefe JA, Nadel L. The Hippocampus as a Cognitive Map. New York: Oxford University Press; 1978.

Olshausen BA, Field DJ. Sparse coding of sensory inputs. Current opinion in neurobiology. 2004; 14:481–487. [PubMed: 15321069]

Palmer LM, Shai AS, Reeve JE, Anderson HL, Paulsen O, Larkum ME. NMDA spikes enhance action potential generation during sensory input. Nature neuroscience. 2014; 17:383–390. [PubMed: 24487231]

Park JY, Remy S, Varela J, Cooper DC, Chung S, Kang HW, Lee JH, Spruston N. A post-burst after depolarization is mediated by group i metabotropic glutamate receptor- dependent upregulation of Ca(v)2.3 R-type calcium channels in CA1 pyramidal neurons. PLoS biology. 2010; 8:e1000534. [PubMed: 21103408]

Park YY, Johnston D, Gray R. Slowly inactivating component of Na+ current in peri-somatic region of hippocampal CA1 pyramidal neurons. Journal of neurophysiology. 2013; 109:1378–1390. [PubMed: 23236005]

Pastalkova E, Itskov V, Amarasingham A, Buzsaki G. Internally generated cell assembly sequences in the rat hippocampus. Science. 2008; 321:1322–1327. [PubMed: 18772431]

Ranck JB Jr. Studies on single neurons in dorsal hippocampal formation and septum in unrestrained rats. I. Behavioral correlates and firing repertoires. Experimental neurology. 1973; 41:461–531. [PubMed: 4355646]

Remy S, Spruston N. Dendritic spikes induce single-burst long-term potentiation. Proceedings of the National Academy of Sciences of the United States of America. 2007; 104:17192–17197. [PubMed: 17940015]

Rich PD, Liaw HP, Lee AK. Place cells. Large environments reveal the statistical structure governing hippocampal representations. Science. 2014; 345:814–817. [PubMed: 25124440]

Royeck M, Horstmann MT, Remy S, Reitze M, Yaari Y, Beck H. Role of axonal NaV1.6 sodium channels in action potential initiation of CA1 pyramidal neurons. Journal of neurophysiology. 2008; 100:2361–2380. [PubMed: 18650312]

Schiller J, Schiller Y, Stuart G, Sakmann B. Calcium action potentials restricted to distal apical dendrites of rat neocortical pyramidal neurons. The Journal of physiology. 1997; 505(Pt 3):605–616. [PubMed: 9457639]

Schmidt-Hieber C, Hausser M. Cellular mechanisms of spatial navigation in the medial entorhinal cortex. Nature neuroscience. 2013; 16:325–331. [PubMed: 23396102]

Segal MM, Douglas AF. Late sodium channel openings underlying epileptiform activity are preferentially diminished by the anticonvulsant phenytoin. Journal of neurophysiology. 1997; 77:3021–3034. [PubMed: 9212254]

Shapiro ML, Eichenbaum H. Hippocampus as a memory map: synaptic plasticity and memory encoding by hippocampal neurons. Hippocampus. 1999; 9:365–384. [PubMed: 10495019]

Smith DM, Mizumori SJ. Hippocampal place cells, context, and episodic memory. Hippocampus. 2006; 16:716–729. [PubMed: 16897724]

Sofroniew NJ, Cohen JD, Lee AK, Svoboda K. Natural whisker-guided behavior by head-fixed mice in tactile virtual reality. The Journal of neuroscience: the official journal of the Society for Neuroscience. 2014; 34:9537–9550. [PubMed: 25031397]

Spruston N, Jonas P, Sakmann B. Dendritic glutamate receptor channels in rat hippocampal CA3 and CA1 pyramidal neurons. The Journal of physiology. 1995; 482(Pt 2):325–352. [PubMed: 7536248]

Stuart GJ, Sakmann B. Active propagation of somatic action potentials into neocortical pyramidal cell dendrites. Nature. 1994; 367:69–72. [PubMed: 8107777]

Stuart GJ, Sakmann B. Amplification of EPSPs by axosomatic sodium channels in neocortical pyramidal neurons. Neuron. 1995; 15:1065–1076. [PubMed: 7576650]

Stuart GJ, Spruston N. Dendritic integration: 60 years of progress. Nature neuroscience. 2015; 18:1713–1721. [PubMed: 26605882]

Stuart GJ, Spruston N, Häusser M. Dendrites. Third. Oxford: Oxford University Press; 2016.

Stuart GJ, Spruston N, Sakmann B, Hausser M. Action potential initiation and backpropagation in neurons of the mammalian CNS. Trends in neurosciences. 1997; 20:125–131. [PubMed: 9061867]

Su H, Alroy G, Kirson ED, Yaari Y. Extracellular calcium modulates persistent sodium current-dependent burst-firing in hippocampal pyramidal neurons. The Journal of neuroscience: the official journal of the Society for Neuroscience. 2001; 21:4173–4182. [PubMed: 11404402]

Taddese A, Bean BP. Subthreshold sodium current from rapidly inactivating sodium channels drives spontaneous firing of tuberomammillary neurons. Neuron. 2002; 33:587–600. [PubMed: 11856532]

Takahashi H, Magee JC. Pathway interactions and synaptic plasticity in the dendritic tuft regions of CA1 pyramidal neurons. Neuron. 2009; 62:102–111. [PubMed: 19376070]

Teles-Grilo Ruivo LM, Mellor JR. Cholinergic modulation of hippocampal network function. Frontiers in synaptic neuroscience. 2013; 5:2. [PubMed: 23908628]

Treves A, Rolls ET. Computational analysis of the role of the hippocampus in memory. Hippocampus. 1994; 4:374–391. [PubMed: 7842058]

Tsodyks MV, Feigelman MV. The Enhanced Storage Capacity in Neural Networks with Low Activity Level. Europhys Lett. 1988; 6:101–105.

Vaidya SP, Johnston D. Temporal synchrony and gamma-to-theta power conversion in the dendrites of CA1 pyramidal neurons. Nature neuroscience. 2013; 16:1812–1820. [PubMed: 24185428]

Wood ER, Dudchenko PA, Eichenbaum H. The global record of memory in hippocampal neuronal activity. Nature. 1999; 397:613–616. [PubMed: 10050854]

Wood ER, Dudchenko PA, Robitsek RJ, Eichenbaum H. Hippocampal neurons encode information about different types of memory episodes occurring in the same location. Neuron. 2000; 27:623–633. [PubMed: 11055443]

Yamada-Hanff J, Bean BP. Persistent sodium current drives conditional pacemaking in CA1 pyramidal neurons under muscarinic stimulation. The Journal of neuroscience: the official journal of the Society for Neuroscience. 2013; 33:15011–15021. [PubMed: 24048831]

Yamada-Hanff J, Bean BP. Activation of Ih and TTX-sensitive sodium current at subthreshold voltages during CA1 pyramidal neuron firing. Journal of neurophysiology. 2015; 114:2376–2389. [PubMed: 26289465]

Zhao X, Liu M, Cang J. Sublinear binocular integration preserves orientation selectivity in mouse visual cortex. Nature communications. 2013; 4:2088.

Ziv Y, Burns LD, Cocker ED, Hamel EO, Ghosh KK, Kitch LJ, El Gamal A, Schnitzer MJ. Long-term dynamics of CA1 hippocampal place codes. Nature neuroscience. 2013; 16:264–266. [PubMed: 23396101]

Highlights

- Steep voltage dependence of responses in place cells is recapitulated *in vitro*
- Subthreshold persistent sodium current (I_{Na-p}) mediates amplification of EPSPs
- I_{Na-p} mediates subthreshold amplification of place-dependent responses *in vivo*
- Synaptic amplification is explained by the biophysics of I_{Na-p} *in silico*

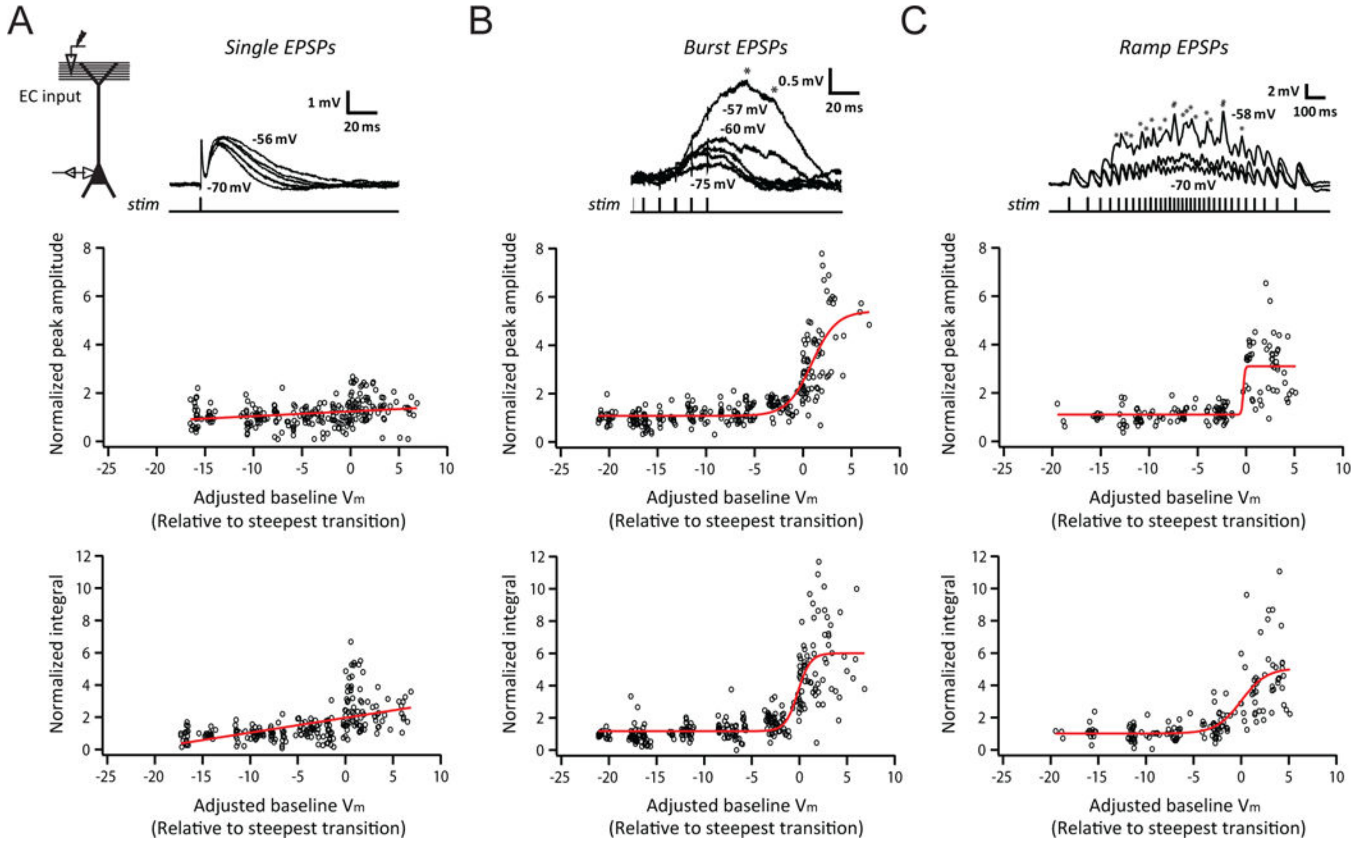

Figure 1. Temporally summated synaptic responses exhibit steep dependence on baseline membrane potential at the soma *in vitro*

(A) Voltage dependence of small, single EPSPs. Experimental configuration (*inset*); representative traces of baseline-subtracted EPSPs at different baseline V_m (indicated for selected traces; *top*); summary of voltage dependence of synaptic responses, showing measures of EPSPs normalized to the average response at or near the resting V_m, plotted as a function of V_m relative to the transition V_m (*bottom*), defined as the baseline V_m which maximized the difference between the means of the measure for all responses above and below the selected V_m (n = 7/7).

(B) As in (A), but for high-frequency synaptic activation (burst of 5 stimuli at 100 Hz; n = 12/11).

(C) As in (A), but for synaptic activation using a train of stimuli at ramp-modulated frequency (n = 9/9).

The average peak response near the resting V_m used in (A) was matched to (B) and (C). Asterisks indicate the timing of removed somatic action potentials. Red lines represent an exponential (A, for which sigmoid fitting did not converge) or a sigmoid (B and C) fit. See STAR Methods for more details. n = neurons/rats. Related data provided in Figure S1.

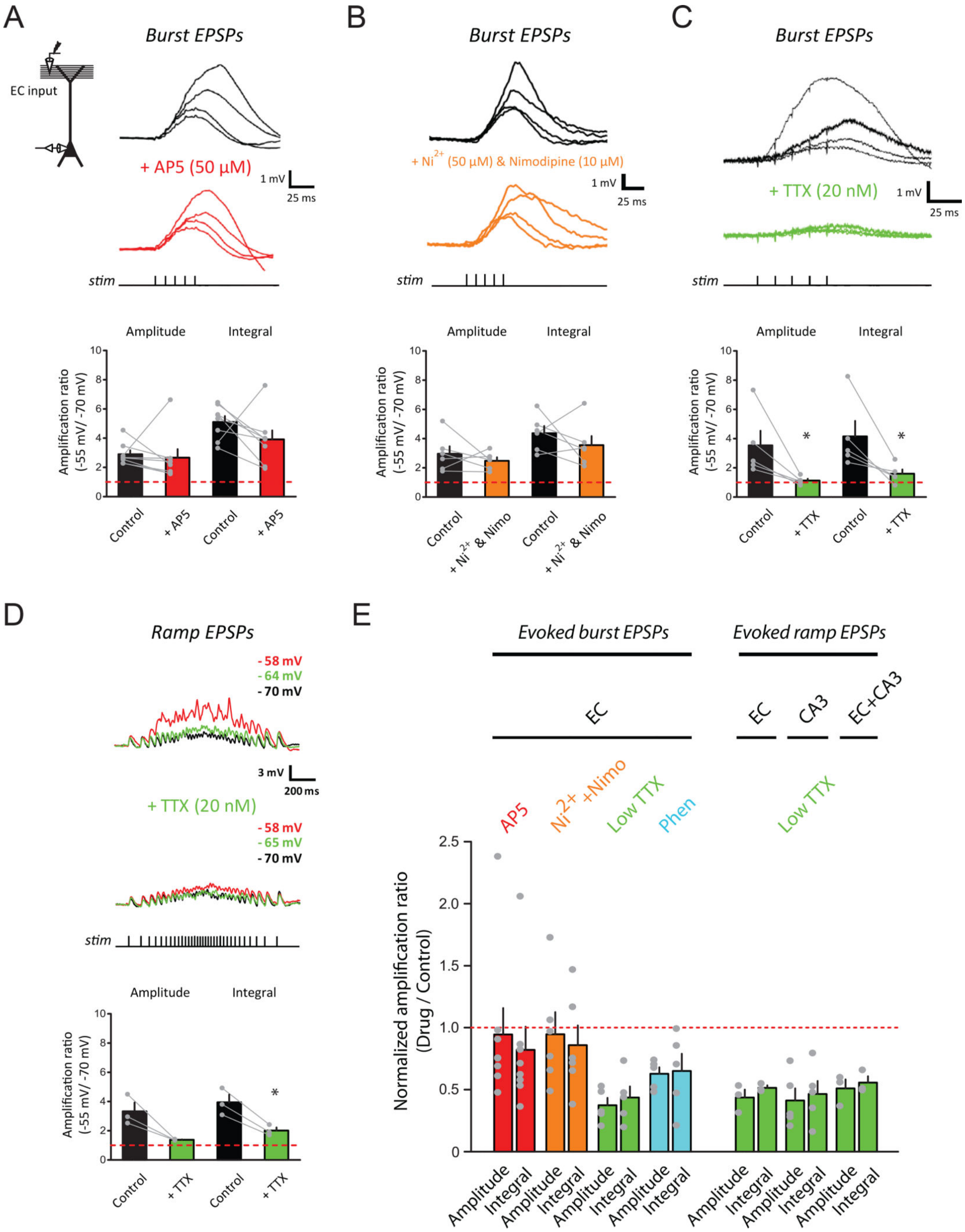

Figure 2. A voltage-gated sodium current critically contributes to the steeply voltage-dependent amplification of temporally summated synaptic responses *in vitro*

(A) Voltage dependence of small, high-frequency burst EPSPs in control, followed by bath application of 50 µM AP5. Experimental configuration (*inset*), representative traces of baseline-subtracted EPSPs at different baseline V_m (*top*), and summary of voltage-dependent amplification (*bottom*; n = 8/6). Dashed line indicates no amplification.

(B) As in (A), but for bath application of 50 µM Ni^{2+} plus 10 µM nimodipine (n = 6/4).

(C) As in (A), but for bath application of low (20 nM) TTX (n = 5/5).

(D) As in (A), but for synaptic activation using a train of stimuli at ramp-modulated frequency in control, followed by bath application of low TTX (n = 3/3). Baseline V_m indicated at top-right.

(E) Amplification ratio for different drug conditions, normalized to the amplification ratio in control. Phen, phenytoin (100 μM).

n = neurons/rats. *$p < 0.05$ by Student's t-test.

Related data provided in Figures S2 and S3.

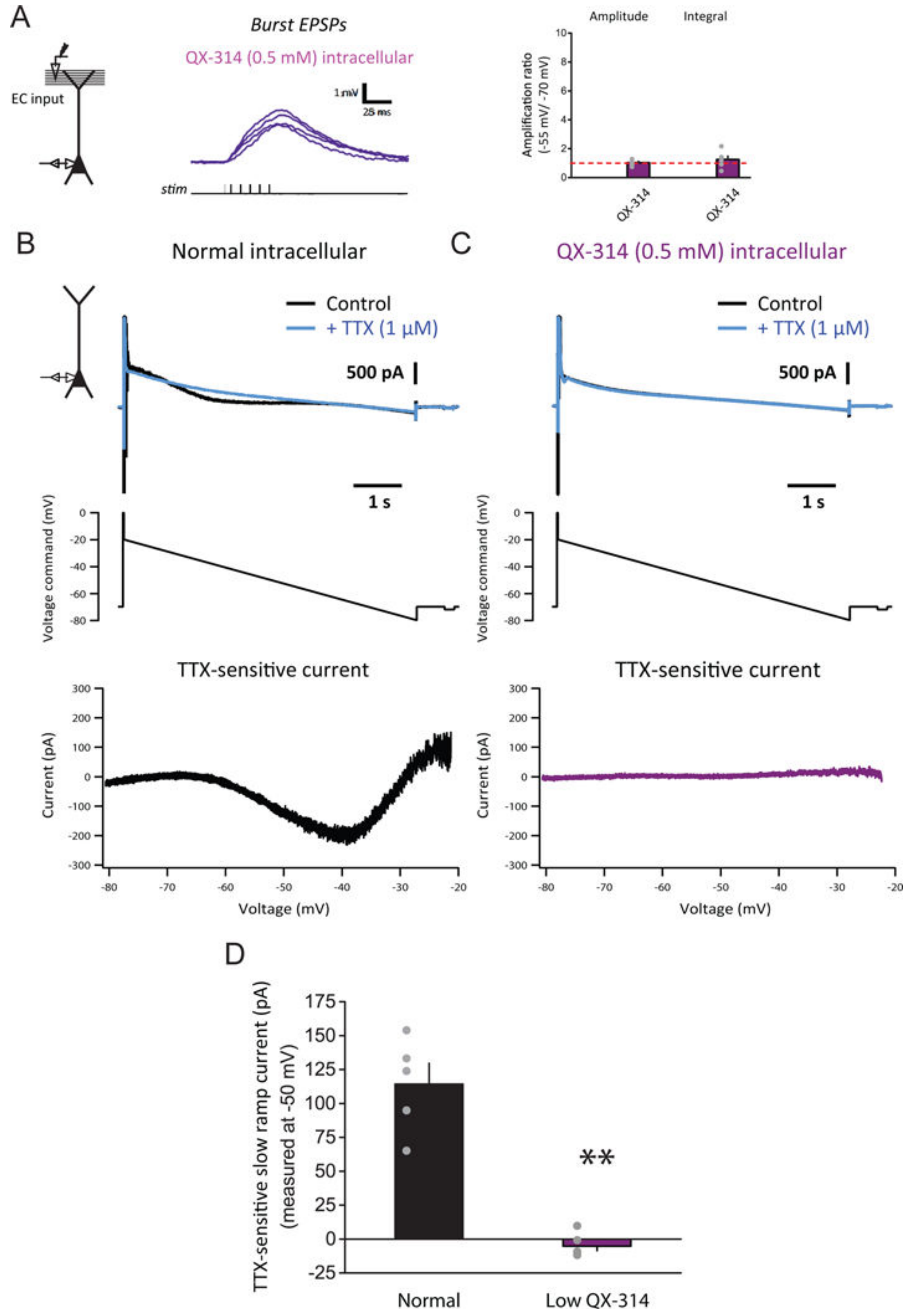

Figure 3. A postsynaptic sodium current activated at subthreshold voltages critically contributes to the steeply voltage-dependent amplification of temporally summated synaptic responses *in vitro*

(A) Voltage dependence of small, high-frequency burst EPSPs with intracellular low (0.5 mM) QX-314. Experimental configuration (*inset*), representative traces of baseline-subtracted EPSPs at different baseline V_m (*left*), and summary of voltage-dependent amplification (*right*; n = 6/6).

(B) Isolation of the nearly non-inactivating voltage-gated sodium current in voltage-clamp recording performed with normal (QX-314-free) intracellular solution. Experimental configuration (*inset*); representative traces of current in control, followed by bath application of 1 μM TTX (*top*); voltage command, consisting of a slow downward ramp (10 mV/s) with a brief pre-pulse (*middle*); I–V curve of TTX-sensitive current (*bottom*).

(C) As in (B), but with intracellular low QX-314.

(D) Summary of effects of intracellular low QX-314 on the nearly non-inactivating voltage-gated sodium current activated at subthreshold voltages in the normal (n = 5/4) or low-QX-314 (n = 6/3) condition. n = neurons/rats. $^{**}p < 0.01$ by Student's t-test.

See STAR Methods for details of experimental design for (B)–(D). Related data provided in Figures S2 and S3.

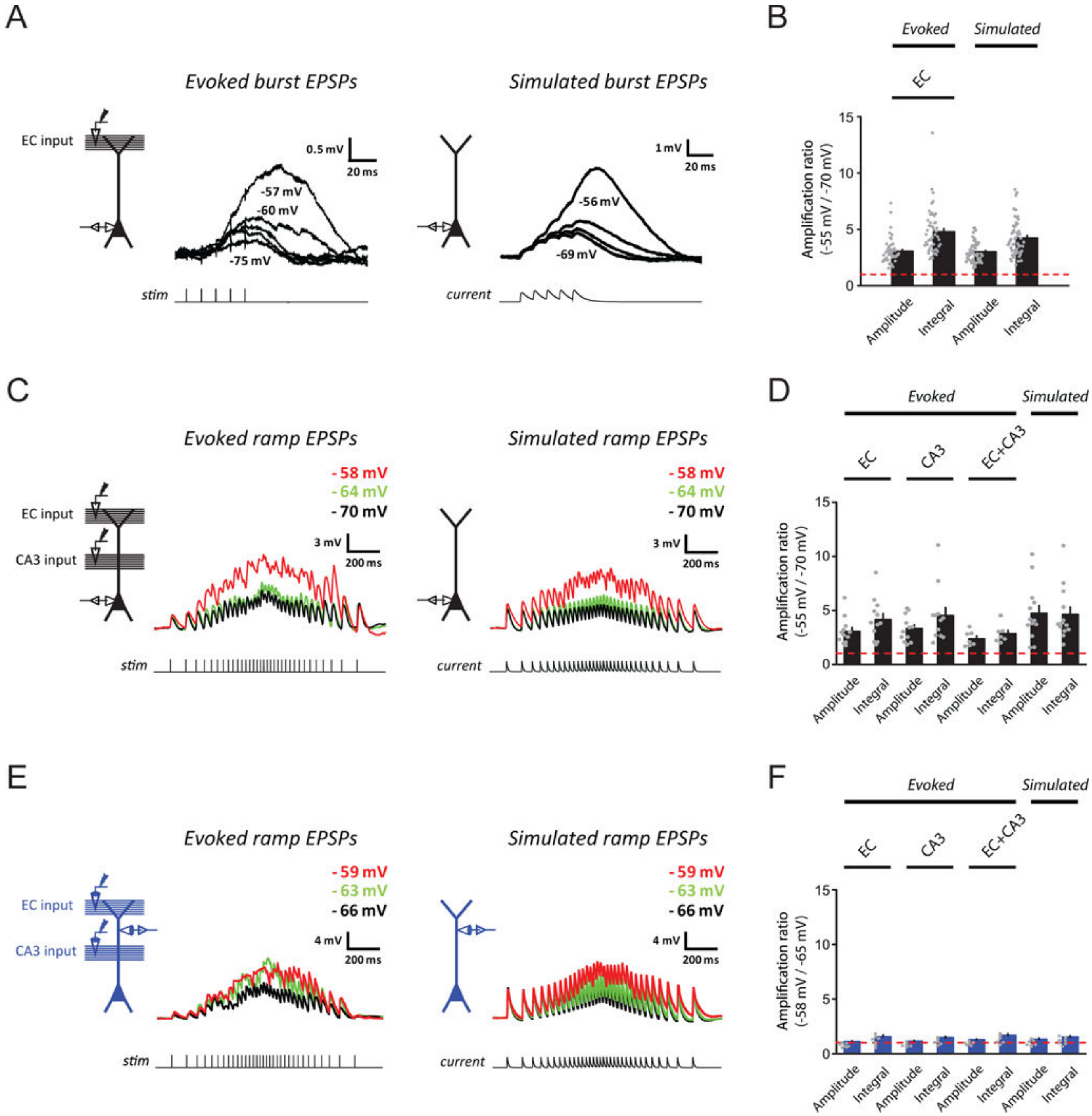

Figure 4. A perisomatic voltage-dependent mechanism supports the steeply voltage-dependent amplification of temporally summated synaptic responses *in vitro*

(A) Examples for voltage dependence of small, synaptically activated (*left*) and simulated (*right*) burst EPSPs in somatic recordings. Experimental configuration (*inset*) and representative traces of baseline-subtracted EPSPs at different baseline V_m (indicated for selected traces).

(B) Summary of voltage-dependent amplification for (A) (evoked, n = 50/41; simulated, n = 55/47). Dashed line indicates no amplification.

(C) As in (A), but for responses at ramp-modulated frequency in somatic recordings. Baseline V_m indicated at top-right.

(D) As in (B), but for (C) (evoked: EC input, n = 12/11, CA3 input, n = 12/11, EC+CA3 inputs, n = 7/6; simulated, n = 13/12).

(E) As in (C), but for dendritic recordings (example recorded 198 μm from the soma).

(F) As in (D), but for (E) (evoked: EC input, n = 7/7, CA3 input, n = 6/6, EC+CA3 inputs, n = 6/6; simulated: n = 7/7).

See STAR Methods and Results for details of experimental design for (E) and (F). n = neurons/rats. Related data provided in Figures S2 and S3.

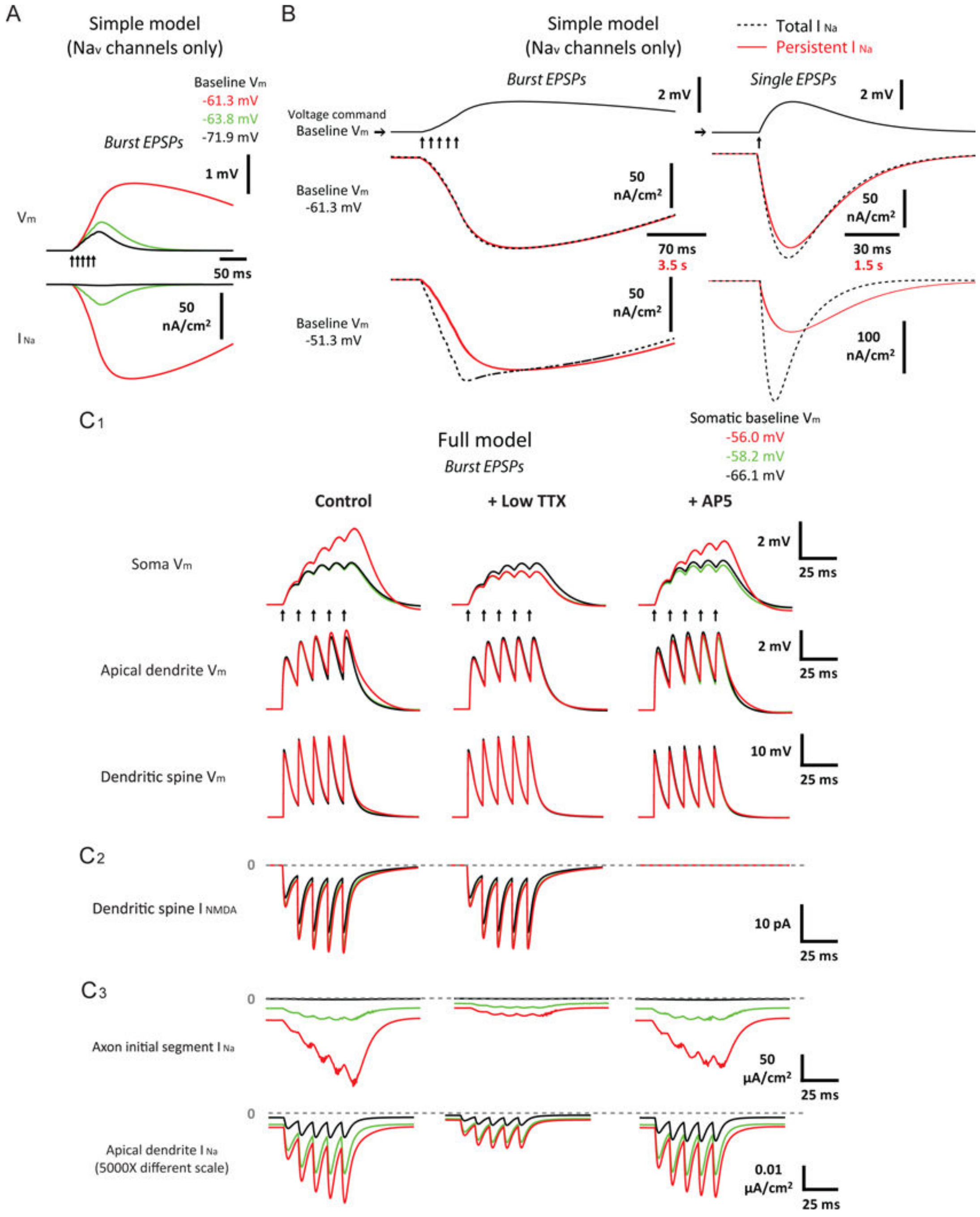

Figure 5. Persistent sodium current mediates steeply voltage-dependent amplification of temporally summated synaptic responses *in silico*

(A) Voltage dependence of small, high-frequency burst EPSPs (5 stimuli at 100 Hz) in a single-compartment model with only standard Na$_v$ channels, constrained to match the measurement of persistent sodium current in CA1 pyramidal neurons. Example traces of baseline-subtracted EPSPs and instantaneous current through Na$_v$ channels (I$_{Na}$) at different baseline V$_m$.

(B) Dependence of difference between total and persistent sodium current on membrane potential and the kinetics of its change in the simple model (same as (A)). Voltage-clamp experiments were simulated using the amplified burst EPSP (the red EPSP trace in (A)) and a single, amplitude-matched EPSP as voltage commands. Baseline V_m was set to a value where synaptic responses were strongly amplified in the model (as shown in (A)) as well as a more depolarized value. Example traces of baseline-subtracted I_{Na} evoked by the real-time ("Total I_{Na}") and the 50X temporally slowed ("Persistent I_{Na}") versions of the EPSP waveforms.

(C) As in (A), but in a biophysically and morphologically detailed model of CA1 pyramidal neurons with standard Na_v channels and *DC* current injected to the soma to modulate V_m, for EPSPs or instantaneous current through Na_v (I_{Na}) or NMDAR (I_{NMDA}) channels recorded from different locations under different simulated drug conditions. The apical dendritic compartment (trunk) and the spine recorded (both 250 μm from the soma) were the same ones across C_1–C_3.

Arrows indicate timing of presynaptic input. See Results and STAR Methods for more details. Related data provided in Figures S4 and S5.

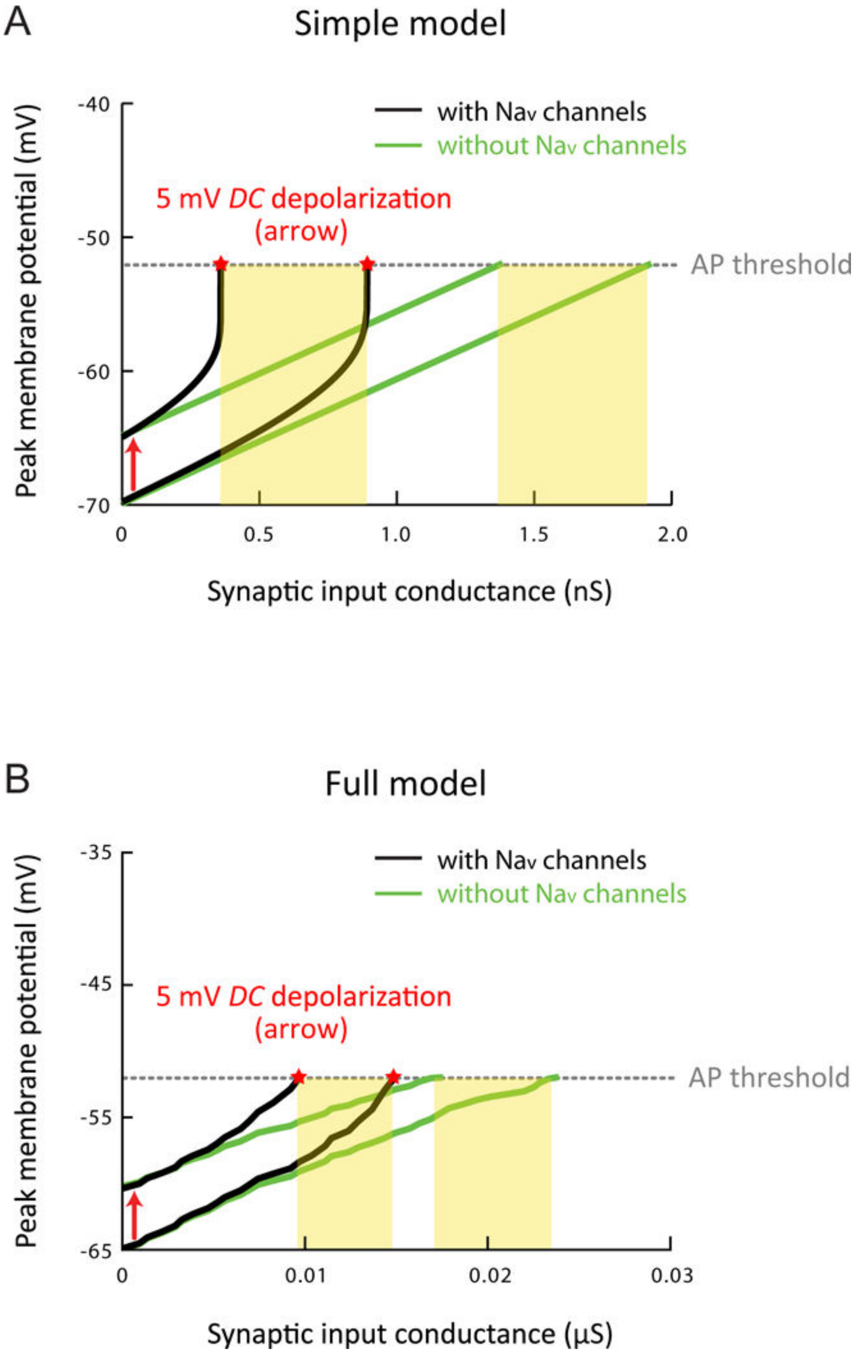

Figure 6. Functional consequences of the steeply voltage-dependent amplification on synaptic integration *in silico*

(A) Effects of persistent sodium current on high-frequency burst EPSPs produced using varying levels of synaptic input in the simple model (same as Figure 5A), showing peak V_m of the response plotted as a function of the conductance of synaptic input at the resting V_m or upon depolarization of V_m by 5 mV in different conditions. Dotted line indicates the apparent voltage threshold for spike initiation in response to the smallest suprathreshold input, in the simulation with Na_v channels performed at the resting V_m. For suprathreshold responses, measurement of peak V_m (indicated by stars) was made just prior to spike initiation. Yellow boxes indicate the range of synaptic conductance for which the depolarization of 5 mV changes the output state of the neuron (i.e., resulting in the peak EPSP that falls above the spike threshold).

(B) As in (A), but in the full model of CA1 pyramidal neurons (same as Figure 5C) with somatic recording and *DC* current injected to the soma to modulate V_m.

Related data provided in Figure S6.

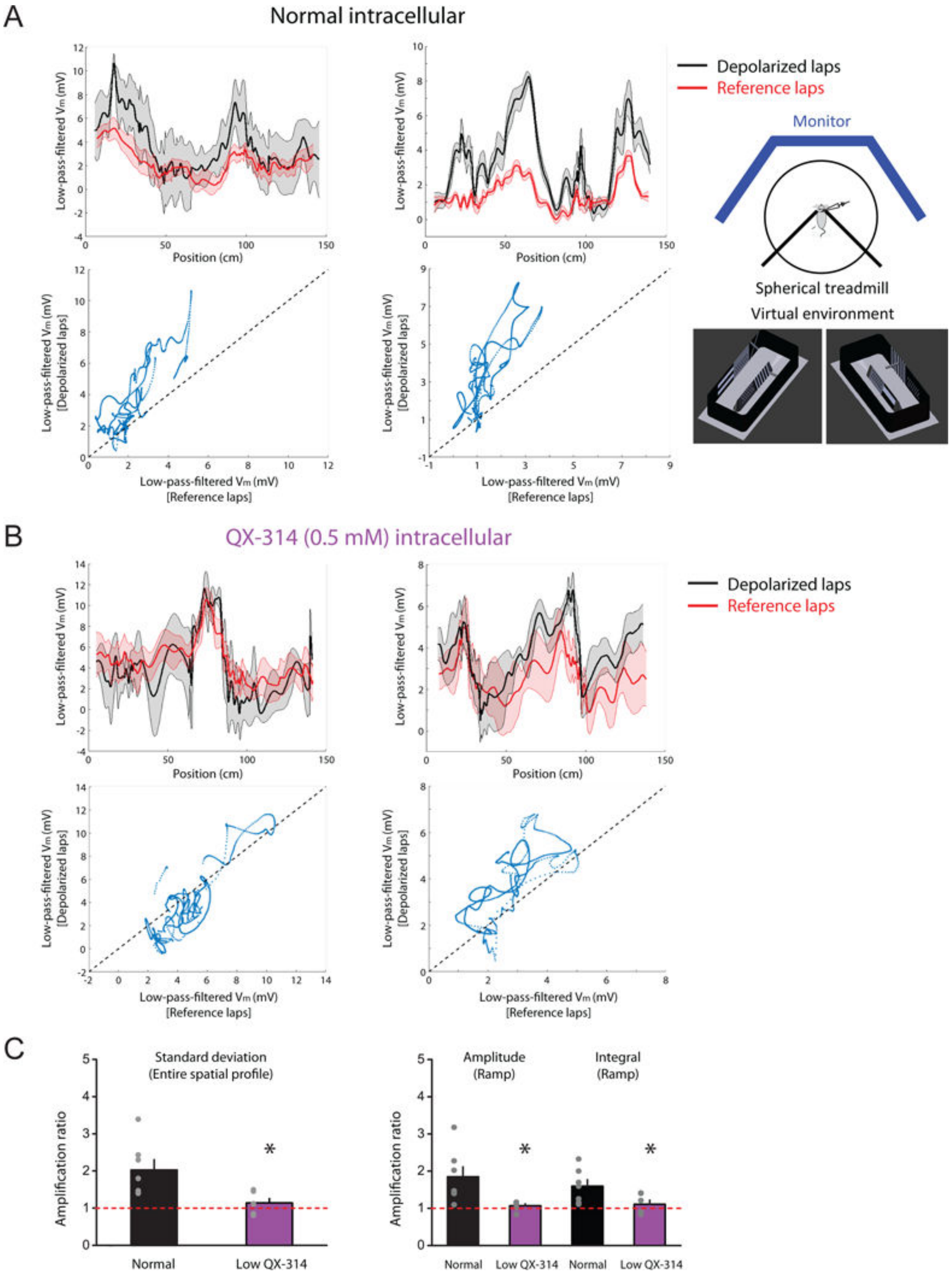

Figure 7. Partial block of postsynaptic Na_V channels significantly reduces voltage-dependent amplification of spatially modulated synaptic responses *in vivo*

Whole-cell recordings in awake mice during virtual navigation.

(A) Two examples (*left* and *right*) for voltage dependence of spatially modulated ramp-like synaptic responses with normal (QX-314-free) intracellular solution. *Inset*, schematic of the experiment setup and two views of the 3-D model for a simulated visual environment. *Top*, baseline-subtracted, 0–2 Hz low-pass-filtered V_m plotted as a function of the animal's linearized position during laps at relatively depolarized ("depolarized laps") and hyperpolarized ("reference laps") V_m. *Bottom*, average low-pass-filtered V_m plotted during depolarized vs. reference laps. Solid lines and shaded areas in the *top* panels represent mean and S.E.M., respectively.

(B) As in (A), but with intracellular low QX-314.

(C) Summary of effects of intracellular low QX-314 on voltage-dependent amplification of spatially dependent synaptic responses, based on the measures of the average spatial V_m profile or spatially modulated synaptic ramps in the normal (n = 7/6) or low-QX-314 (n = 6/6) condition.

n = neurons/mice. *$p < 0.05$ by Student's t-test.

See STAR Methods for more details. Related data provided in Figure S7.

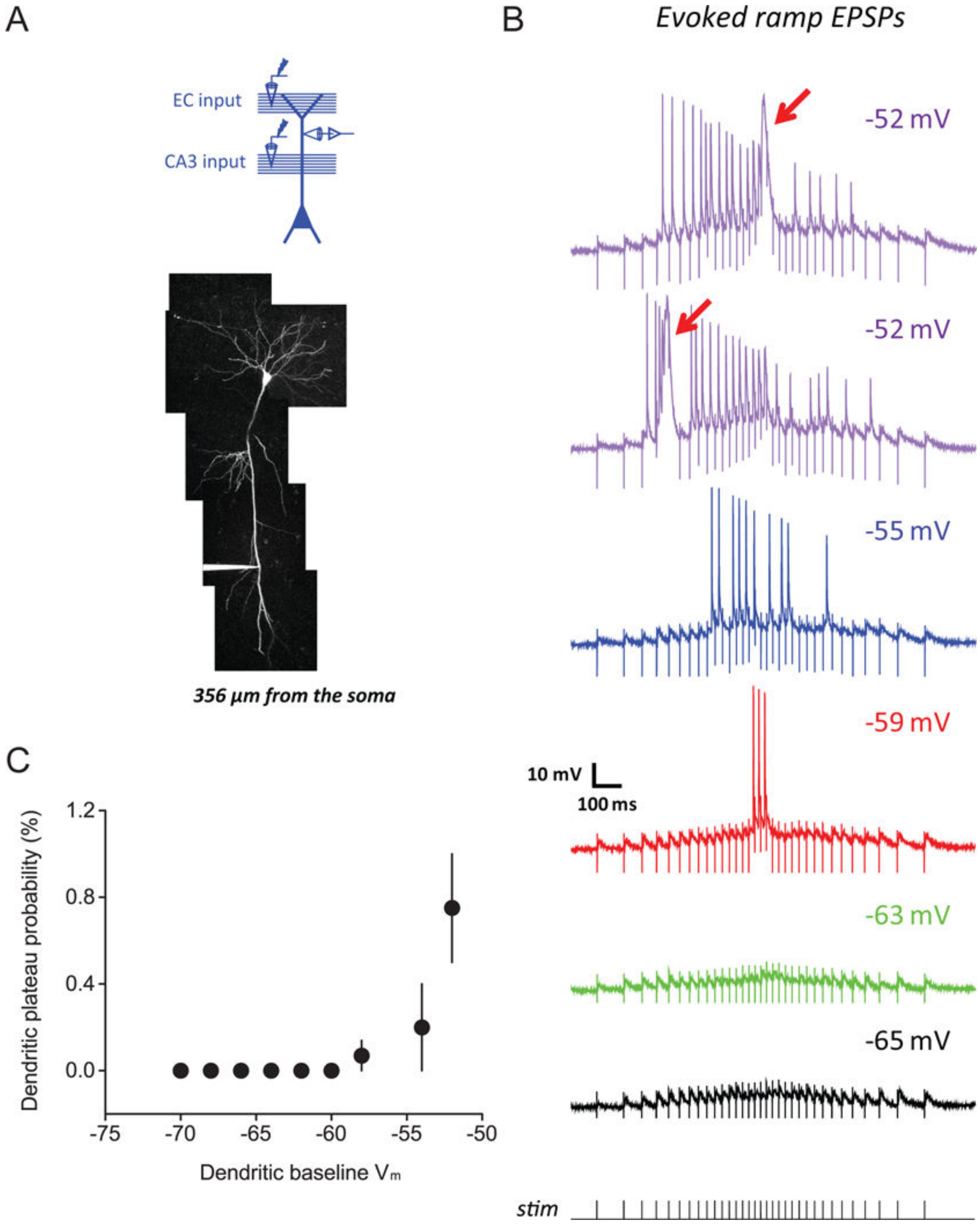

Figure 8. Voltage-dependent synaptic amplification mediated by dendritic plateau potentials requires relatively strong dendritic depolarization

(A) Experimental configuration (*top*) and Z-stack image of a dendritically recorded neuron (filled with 50 µM AF-594; *bottom*)

(B) Representative example for voltage dependence of dendritic responses for synaptic activation using a train of stimuli at ramp-modulated frequency, tested at dendritic baseline V_m (indicated at top-right) covering a more depolarized range (than tested in Figure 4E, F, S3A, see Results for details of experimental design). Arrows indicate dendritic plateau potentials.

(C) Summary of effects of dendritic depolarization on dendritic plateau potentials in response to coincident EC and CA3 inputs at ramp-modulated frequency, showing the probability of observing plateau potentials in dendritic recordings (“dendritic plateau probability”; see STAR Methods) plotted as a function of dendritic baseline V_m (n = 7/7).
n = neurons/rats.
Related data provided in Figure S8.